ALMA MATER STUDIORUM
UNIVERSITÀ DI BOLOGNA

DEPARTMENT OF PHYSICS AND ASTRONOMY ”A. RIGHI”

SECOND CYCLE DEGREE

PHYSICS

First transmission measurement at n_TOF: determination of the ^{nat}Cu total cross section over a wide energy range

Supervisor

Prof. Cristian Massimi

Co-supervisors

Dr. Donato Maurizio Castelluccio
Dr. Alice Manna
Dr. Nicholas Pieretti

Defended by

Alice Berardi

Graduation Session February 2026

Academic Year 2025/2026

Abstract

Accurate and precise nuclear data are essential for the design, safety assessment, and performance evaluation of advanced nuclear energy technologies, particularly Generation IV fission and fusion reactors. In this context, copper plays a key role in systems such as the TAPIRO fast-spectrum research reactor, where sensitivity studies have shown a strong dependence on neutron-induced copper cross sections. However, the available experimental data for copper are scarce and significant inconsistencies exist among evaluated nuclear data libraries.
To address these limitations, an experimental measurement campaign was proposed, including measurements at the n_TOF facility at CERN to improve neutron-induced copper cross sections. While radiative capture cross section measurements for ^{63}Cu and ^{65}Cu have already been performed, this thesis presents the measurement and analysis of the total cross section of ^{nat}Cu carried out in 2025 at n_TOF. It consisted of a transmission measurement, one of the first ever performed at the n_TOF facility. The experiment was carried out in the EAR1 experimental area, using a natural copper sample and a Low Mass Fission Chamber as a transmission detector.
A comprehensive data analysis is presented, involving optimization studies aimed at improving data quality, so as to extract accurate ^{nat}Cu(n,tot) cross section.

Thanks to the broad neutron energy spectrum available at the n_TOF facility, the extracted ^{nat}Cu(n,tot) cross section covers a wide energy range, from meV extending up to 30 MeV. The results are in agreement with the limited experimental data reported in the literature and evaluated nuclear data libraries, especially in the resonance region, confirming the quality of the measurements and the robustness of the analysis procedure.

Contents

Introduction

The accurate and precise knowledge of nuclear data is essential for a wide range of applications in nuclear physics and engineering. In particular, nuclear reactors play a central role in the context of the growing global demand for reliable and low-carbon energy sources. Among reactor technologies, Generation IV fission reactors and nuclear fusion reactors represent the most advanced and innovative concepts, as they are designed to significantly improve safety, sustainability, and efficiency in energy production. Despite the intense research and development efforts, with the involvement of large international collaborations, these reactor technologies still have very limited operational experience, with only a few prototypes built worldwide. Unlike previous reactor generations, which benefit from decades of operational feedback, advanced reactor systems must rely predominantly on predictive modeling and simulations, making the availability of high quality nuclear data even more critical.

The process that prepares nuclear data for their use in applications is a complex, multi-step process that begins with experimental measurements and proceeds through data evaluation and validation. Being the foundation of the nuclear data pipeline, experimental data must be highly accurate, since even small systematic biases can propagate through the entire pipeline and lead to significant consequences for the applications. For this reason, sensitivity and uncertainty analyses are performed to quantify the impact of nuclear data uncertainties on application-relevant quantities, such as integral reactor parameters. Studies of this type were also conducted for TAPIRO, a low power fast spectrum research reactor operated by ENEA in Casaccia, employed for nuclear data production, validation of calculation codes for Generation IV reactors, and investigations of fast-neutron-induced damage. These studies have shown that TAPIRO is particularly sensitive to neutron-induced cross sections of copper, which is used in the reflector and in the control rods. A review of the current state of the art indicates that experimental nuclear data for copper are scarce and that evaluated nuclear data libraries show significant inconsistencies for the isotopes $^{63}\mathrm{Cu}$ and $^{65}\mathrm{Cu}$. These limitations, together with the strong relevance of copper data for the TAPIRO reactor, motivated the proposal of an experimental campaign aimed at refining neutron-induced copper cross sections. This campaign, jointly proposed by ENEA and INFN within the Euratom-funded APRENDE project, was named RAMEN and it involves experimental measurements of copper cross sections at the n_TOF facility at CERN. Capture cross sections were measured in 2024 and their data analysis is currently in progress. In 2025, total cross sections were measured by means of a transmission experiment, constituting one of the first experiments of this kind performed at n_TOF.

This thesis presents the transmission experiment of natural copper carried out at n_TOF, along with the data analysis which involved optimization studies to extract ac-

curate total cross section from the data acquired during the campaign.
Chapter 1 illustrates the applications of copper nuclear data and highlights the importance of accurate cross section data. Chapter 2 provides an overview of the n_TOF facility, describing the Time-of-Flight (TOF) method and the characteristics that make n_TOF one of the most important facilities worldwide for nuclear data production. In Chapter 3, the transmission experiment of natural copper is presented. A description of the principles of transmission measurements is provided, followed by details on the experimental setup and the measurement campaign. Finally, Chapter 4 describes the data analysis procedure that led to the extraction of the total cross section over the full neutron energy range.

1 Relevance of Copper nuclear data

Nuclear reactor technologies stand out for their strong potential to support decarbonization while ensuring stable and large-scale energy production. In this context, the fourth generation nuclear fission reactors, together with nuclear fusion reactors, represent the most advanced and innovative technologies. An overview of these technologies is presented in Section 1.1.
The nuclear data used in the applications is actually the result of a complex process, that brings together international efforts for the production of high-quality datasets. The entire nuclear data pipeline, starting from experimental measurements, passing through evaluation and validation, and finally leading to the preparation of data libraries for practical applications, is described in Section 1.2.
Section 1.3 presents the TAPIRO ENEA-Casaccia research reactor, an important facility for experimental activities devoted to nuclear data production, validation of calculation codes for Generation IV reactors, and studies of fast-neutron-induced damage, among other applications. This reactor is particularly sensitive to copper nuclear data, especially neutron-induced cross sections, as discussed in Section 1.3.1. For the safety and reliability assessment of TAPIRO, as well as for other systems that exploit similar technologies, an accurate knowledge of nuclear copper data is therefore essential.
Finally, Section 1.4 describes the state of the art of Cu(n,tot) cross section, both in terms of experimental and evaluated data. The scarcity and inconsistency observed in the available data motivated the proposal of an experimental campaign aimed at refining copper nuclear data, named RAMEN, which includes the experiment presented in this thesis and is described in Section 1.5.

1.1 IV Generation and Fusion Nuclear Reactors

In this section, a short overview of the main features of the next generation fission and fusion reactors is presented.

IV Generation nuclear fission reactors Generation IV nuclear reactors represent an evolution with respect to previous nuclear power systems, aiming to address some of the fundamental limitations of current technologies. While earlier generations of reactors were mainly focused on reliable electricity production and incremental safety improvements, Generation IV reactors introduce more innovative approaches to fuel utilization, safety, and energy efficiency. Generation IV does not correspond to a single reactor type, but rather to a class of innovative systems based on advanced design concepts, materials, and fuel cycle strategies. An international collaboration aimed at coordinating research and development of next-generation nuclear fission systems was established in 2001: the Gen IV International Forum (GIF) [1].

GIF has established technology goals for Gen-IV systems in four broad areas: sustainability, economics, safety and reliability, and proliferation resistance and physical protection [2]. These ambitious goals are shared by a large number of countries as they aim at responding to the economic, environmental and social requirements of the 21st century. They establish a framework and identify concrete targets for GIF R&D efforts. In the area of sustainability, Gen IV systems are expected to provide long-term, clean energy generation with effective fuel utilization and minimized nuclear waste, thereby reducing the burden of long-term stewardship and enhancing environmental protection. From an economic standpoint, these systems aim to achieve life-cycle cost competitiveness with other energy sources while maintaining financial risk levels comparable to other large energy projects. Furthermore, Generation IV nuclear energy systems operations are expected to excel in safety and reliability. They will have a very low likelihood and degree of core damage and eliminate the need for offsite emergency response. Finally, proliferation resistance and physical protection goals strive to make Gen IV technologies unattractive pathways for diversion or theft of weapons-usable material and to provide increased protection against acts of terrorism. These concrete targets are intended to ensure that future nuclear energy systems not only bring technical advancements, but are also socially and politically acceptable, reinforcing international cooperation toward their eventual deployment.
The goals adopted by GIF provided the basis for identifying and selecting six nuclear energy systems for further development. The selected technologies are: Sodium-cooled Fast Reactor (SFR), Gas-cooled Fast Reactor (GFR), Lead-cooled Fast Reactor (LFR), Molten Salt Reactor (MSR), Supercritical Water-cooled Reactor (SCWR) and Very High Temperature Reactor (VHTR). An overview of the six selected technologies, along with their plant schemes, is presented in Figure 1, while Table 1 reports their main characteristics.
These systems differ in neutron spectrum, coolant type, outlet temperature, fuel cycle approach, and power output, reflecting a diversity of design strategies aligned with

System	**Neutron spectrum**	**Coolant**	**Outlet T (°C)**	**Fuel cycle**	**Size (MWe)**
VHTR	Thermal	Helium	900–1000	Open	250-300
SFR	Fast	Sodium	500–550	Closed	up to 1500
SCWR	Thermal / fast	Water	510–625	Open / closed	up to 1500
GFR	Fast	Helium	850	Closed	$\sim$ 1200
LFR	Fast	Lead	480–570	Closed	up to 1200
MSR	Thermal / fast	Fluoride salts	700–800	Closed	300-1000

Table 1: Main features of the six Generation IV reactor systems selected by the GIF [2].

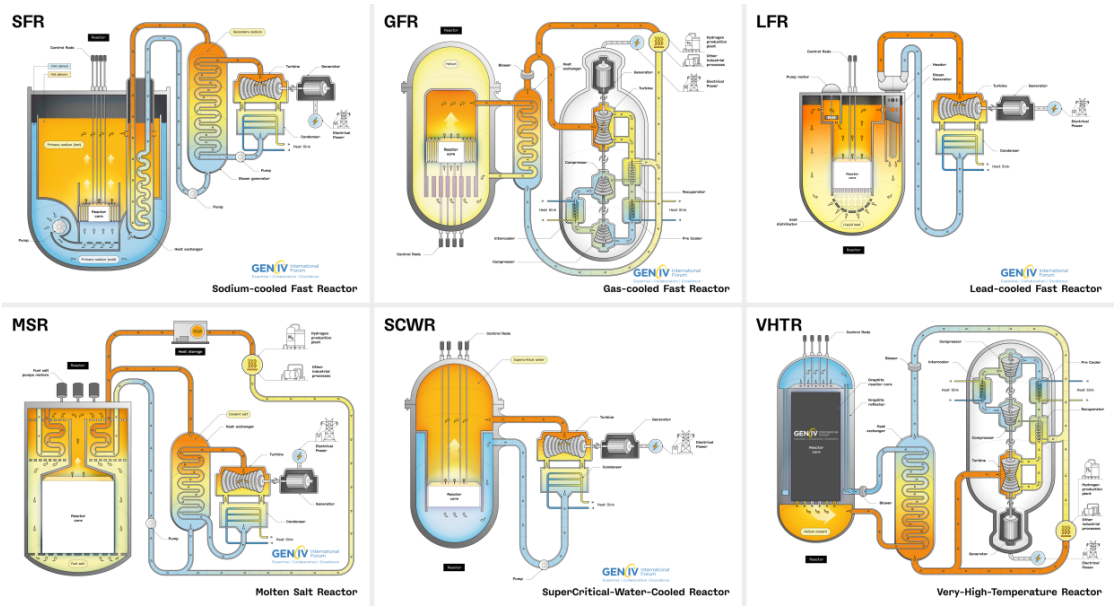

Figure 1: Schematic representation of the six Generation IV reactor technologies selected by the Generation IV International Forum: Sodium-cooled Fast Reactor (SFR), Gas-cooled Fast Reactor (GFR), Lead-cooled Fast Reactor (LFR), Molten Salt Reactor (MSR), Supercritical Water-cooled Reactor (SCWR) and Very High Temperature Reactor (VHTR) [3].

different operational goals.

The VHTR is characterized by a thermal neutron spectrum and helium coolant, achieving outlet temperatures up to about 1000° C, sufficient to support high temperature processes such as the production of hydrogen by thermo-chemical processes. The GFR also uses helium as coolant but operates with a fast neutron spectrum and a closed fuel cycle, targeting higher fuel efficiency. The use of dense fuel such as carbide or nitride provides good performance regarding plutonium breeding and minor actinide burning. SFR and LFR utilize liquid metal coolants, sodium and lead respectively, allowing high power density with low coolant volume fraction. They operate in the fast neutron spectrum with closed fuel cycles, allowing fuel breeding and actinide burning. The MSR employs fluoride salt coolant and can operate in either thermal (with a thorium fuel cycle) or fast spectrum (with a Uranium-Plutonium fuel cycle). Finally, the SCWR is a high-temperature, high-pressure water-cooled reactor operating with a direct energy conversion cycle and above the thermodynamic critical point of water. A wide variety of designs are currently considered for this technology, with both thermal-neutron and fast-neutron spectra being envisaged and supporting both open and closed fuel cycles.

This diversity illustrates the multifaceted approaches within Generation IV to optimize reactor performance, safety, and fuel sustainability across different technological pathways.

Nuclear fusion reactors Nuclear fusion is widely pursued as a long-term solution for low-carbon, large-scale energy production, offering a fundamentally different approach compared to fission. Fusion reactions, such as deuterium–tritium fusion, have the potential to generate substantial amounts of energy from fuels that are abundant and widely available. Deuterium can be extracted from seawater in large quantities, and tritium can be bred in situ from lithium using fusion neutrons, reducing dependence on limited fuel resources and enhancing energy sustainability over long time scales [4].

One of the key motivations for fusion research is the prospect of a virtually inexhaustible fuel supply combined with low environmental impact. Fusion processes do not produce greenhouse gases during operation and generate only modest levels of long-lived radioactive waste compared to fission, with most activation arising from structural materials exposed to high-energy neutrons rather than from the fusion reaction itself. Moreover, fusion reactors inherently avoid chain reactions and the risk of runaway accidents, as the plasma conditions required for fusion are difficult to sustain without precise control. Fusion research also aligns with safety and proliferation resistance objectives. Since fusion cores do not utilize fissile materials like Uranium-235 or Plutonium, they present a lower risk in terms of nuclear weapons proliferation. In the event of system failure, the plasma rapidly cools and extinguishes, minimizing the potential for radiological release. Advances in materials science, particularly low-activation structural materials, are crucial to ensuring that activated components can

be managed safely over the reactor's lifetime.

Two main technologies are currently under development for confining the plasma to achieve fusion: Magnetic and Inertial Confinement [5].
Magnetic confinement uses strong magnetic fields to confine hot plasma in toroidal devices, achieving a long confinement time for low-density fuel. Tokamaks are the most advanced concept of this type, with the International Thermonuclear Experimental Reactor (ITER) [6] under construction in France as the flagship project, involving 34 countries. As an alternative magnetic confinement concept, stellarators use complex three-dimensional magnetic field geometries to confine plasma without relying on large plasma currents.
The inertial confinement, on the other hand, creates plasma by compressing and heating tiny fuel pellets by high-power lasers. In this case, the plasma has a high density at the expense of a shorter confinement time. An experimental facility that makes use of this technology is the National Ignition Facility (NIF) in the United States. Recent experiments at NIF have demonstrated energy yields exceeding the input laser energy for the fusion reaction itself, marking important scientific milestones toward ignition and energy gain, although significant engineering challenges remain before this method can be scaled to continuous power production.

Despite the attractive features of fusion energy and the global efforts that are undergoing for its development, there are still major technical challenges that need to be addressed. The extreme temperatures, particle fluxes, and neutron environments required for sustained fusion place stringent demands on confinement systems and reactor components. Key challenges include managing intense heat loads on plasma-facing materials, breeding and handling tritium efficiently, and ensuring long-term structural integrity under neutron irradiation.

Both Generation IV fission and fusion reactors make significant use of copper because of its excellent thermal and electrical conductivity. An example of a fast research reactor that extensively employs copper is TAPIRO, described in Section 1.3, whose control rods and reflector are made of natural copper. In fusion reactors, copper is widely used, particularly in tokamaks heat sink components, such as the first wall and divertor, as well as magnets, diagnostic systems, microwave waveguides and mirrors [7].

1.2 The Nuclear data pipeline

Robust, high-quality nuclear data, in terms of precision and accuracy, underpin progress in nuclear technology and related applications [8]. In practice, outdated, imprecise or incomplete nuclear datasets can hinder progress, constrain achievable predictive evaluations and, when safety margins are involved, compromise confidence in design and licensing analyses. This need is especially acute for advanced nuclear systems such as Gen IV and fusion reactors, for which there is scarce operational experience (see Section 1.1). Unlike earlier reactor generations, whose design and optimization benefited from decades of experimental experience and in-service performance data, the development of advanced reactors depends more heavily on predictive modeling, making the high accuracy and completeness of nuclear data a fundamental requirement.

The production of increasingly refined nuclear datasets, improving both precision and accuracy, relies on a structured multi-stage process, whose stages are tightly interconnected [9]. Transforming raw experimental measurements into application-ready datasets requires several interdependent steps, often referred to collectively as the nuclear data pipeline.

Experimental measurements The nuclear data pipeline is typically initiated by identifying a specific data need: gaps across the energy range of interest, inconsistencies among the available datasets, excessive uncertainties (compared to the accuracy required for the intended application), or insufficient precision. These issues are revealed by applications and validation studies and are then translated into a justified proposal for new or improved measurements. Initiatives such as the OECD-NEA High Priority Request List (HPRL) [10] can help structure this step by documenting what data are needed, why they matter for applications, and how new measurements would reduce key uncertainties — thereby providing a basis for prioritising experimental campaigns. In practice, proposals are not necessarily channelled through the HPRL, but an HPRL recommendation (or the assessment of the relevant expert group) is often cited to strengthen the motivation and to demonstrate the broader, internationally recognised relevance of the requested measurements when seeking access to major laboratory facilities. Once the need is defined and an experimental program duly justified and motivated, the pipeline proceeds with new differential measurements carried out at one of the dedicated, qualified facilities operated worldwide by major research laboratories.

Compilation Once a measurement campaign has been completed and the results have been documented, a compilation stage ensures that the information becomes findable, traceable, standardised, and reusable by the wider community. In practice, compilation proceeds through two complementary layers. First, the Nuclear Science References (NSR) database provides a continuously updated bibliographic index of nuclear-science literature—journal articles, conference proceedings, laboratory reports, theses,

and related sources—classified and keyworded to support efficient retrieval and subsequent evaluation activities [11].

Building on the primary references catalogued in NSR, numerical experimental results for nuclear reactions — including reported mean values, associated uncertainties, and essential experimental metadata — are extracted by the international nuclear data centres and compiled into the Experimental Nuclear Reaction Data Library (EXFOR) [12]. EXFOR is the principal global repository for experimental nuclear reaction data induced by incident neutrons, charged particles, and photons. It contains reaction cross sections and a broad set of related observables, such as resonance parameters and integrals, fission yields, angular-distribution and polarisation information, spectra, and other quantities relevant to nuclear data evaluation and applications. By preserving structured experimental descriptions and explicit links back to the original publications, EXFOR provides the traceability and standardisation needed for long-term usability.

Evaluation The next step of the nuclear data pipeline is evaluation. In essence, nuclear data evaluation seeks the maximum possible coherence between information derived from experiments and that provided by theory and modeling [13]. Starting from experimental datasets compiled in EXFOR, evaluators critically assess the available measurements, resolve or rationalise inconsistencies, and use nuclear-reaction and nuclear-structure models - together with systematics and physical constraints - to provide a complete and self-consistent description of the required observables. This modeling support is indispensable because only a fraction of the quantities needed in a general-purpose library can be obtained directly from measurements; models and codes are therefore used both to fill gaps and to enforce overall consistency across reaction channels and energy ranges. By integrating experimental results with theoretical predictions, evaluation produces continuous evaluated files that cover the full energy range of interest for applications. These libraries result from a rigorous assessment process, in which evaluators analyze, compare, and combine all available datasets, select (and, where necessary re-normalise) the most reliable inputs, and establish a coherent set of standardized reference data, which constitute the evaluated nuclear data libraries [14]. In modern evaluation practice, this step increasingly includes not only best-estimate values but also a structured quantification of uncertainties and, where available, covariance information to support uncertainty propagation in simulations. Evaluation activities are organised within the major national and international programmes, and coordinated through frameworks such as the OECD-NEA Working Party on International nuclear Data Evaluation Co-operation (WPEC). Prominent evaluated nuclear data library projects include the U.S. ENDF/B library (produced and recommended by CSEWG and distributed via the National Nuclear Data Center), the European JEFF library (a collaboration among NEA Data Bank participating countries), as well as JENDL (Japan), CENDL

(China), and ROSFOND/BROND (Russia).

These libraries typically provide evaluated reaction cross sections, energy and angular distributions of emitted particles, fission product yields, radioactive decay data, photo-atomic data, and thermal scattering law data, with a strong emphasis on neutron-induced reactions. To ensure interoperability with processing systems and application codes, the evaluated information is distributed in the internationally adopted ENDF-6 format, maintained under CSEWG stewardship.

Processing Data stored in evaluated libraries are not yet directly usable by most nuclear application codes. The processing phase converts evaluated, "physics-native" evaluations (typically distributed in ENDF format) into code-ready libraries tailored to specific transport tools. In practice, this conversion is performed with dedicated processing tools - like NJOY, or FRENDY - whose mission is precisely to take the basic evaluate information and generate the representations required by a given application. Processing (or preparation) is more than a file-format translation: it applies a sequence of physics - and numeric-driven transformations that depend on:

- how the evaluation was constructed, (e.g., resonance parametrisation and model assumptions),
- the limitations and conventions of intermediate formats used during processing,
- the requirements of downstream codes (continuous-energy Monte Carlo vs multigroup deterministic transport; depletion/activation coupling; thermal scattering treatment; temperature grids; self-shielding approaches).

Typical operations include resonance reconstruction and linearisation, Doppler broadening to application temperatures, unresolved-resonance probability table generation, thermal scattering law treatment, and the generation of either continuous-energy interfaces (e.g., ACE) or multigroup, self-shielded libraries and standard interfaces.

Finally, preparation is tightly linked to verification and validation. Integral benchmarks and code-to-experiment (C/E) comparisons are performed with "prepared" libraries, so discrepancies can originate not only from the underlying evaluation but also from processing choices or implementation details. For this reason, modern validation workflows explicitly include processed-library verification and controlled benchmarking as integral steps in assessing nuclear data performance.

Validation The validation stage of the nuclear data pipeline is essential to demonstrate that evaluated data - once processed in application libraries - can reliably reproduce the physical behaviour of nuclear systems in simulations. Validation relies on integral benchmark experiments, namely well-characterized reference configurations performed at dedicated facilities, for which integral responses (such as spectral indices,

reactivity effects, kinetic parameters, reaction-rate ratios, k_{eff}, etc.) are determined together with defensible high precision measurements. The same integral observables can be computed through simulations of these benchmark configurations using the processed evaluated data as input. A consistent comparison between calculated and measured benchmark results provide an objective basis for assessing the performance, reliability, and practical adequacy of the nuclear data in conditions representative of real applications. Complementing these, SINBAD (Shielding Integral Benchmark Archive and Database) preserves and standardises radiation shielding and dosimetry benchmark experiments relevant to reactor shielding, fusion neutronics, and accelerator shielding. Two OECD-NEA programs, the International Reactor Physics Experiment Evaluation Project (IRPhEP) and the International Criticality Safety Benchmark Evaluation Project (ICSBEP) [15], produce peer-reviewed handbooks containing evaluated integral benchmark data, which are extensively used for nuclear data benchmarking. This systematic availability of high-quality integral benchmarks is a cornerstone for continuous improvement for major evaluated nuclear data libraries (ENDF/B, JEFF, JENDL, CENDL, etc.) that are used for nuclear analyses [16].

Applications Finally, the validated nuclear data files are deployed across a broad spectrum of applications, including reactor design and safety analysis, criticality safety, nuclear astrophysics, radiation shielding, dosimetry and medical physics.
The emergence of innovative technologies, or the introduction of more stringent accuracy requirements often exposes limitations in current datasets, triggering the need for refined or additional nuclear data. In such instances, the nuclear data pipeline is dynamically reactivated, initiating a new cycle of experimental measurements, evaluations, and validation activities. Consequently, applications do not merely represent the endpoint of the nuclear data production chain, but serve as a critical feedback mechanism that drives continuous evolution. By identifying gaps and setting new standards, the application layer ensures the constant improvement of the quality, reliability, and precision of the entire nuclear data ecosystem.

The entire nuclear data pipeline relies on the experimental nuclear data on which it is built. Any bias, missing effect, or underestimated uncertainty in the differential measurements can propagate downstream -through compilation and evaluation, into processed application libraries, and finally into validation results - thereby affecting the credibility of the simulations and the decisions based on them.

In fact, even for modern libraries, only a limited subset of required quantities can be constrained directly by measurements; nevertheless, experimental data provide the indispensable anchor that guides evaluators and constrains model-based completions.

A practical consequence is that seemingly modest deficiencies at the differential-data level can translate into non-negligible effects on integral reactor parameters. For

example, a small systematic bias in a key reaction cross section may induce a measurable deviation in calculated k_{eff} of in other integral responses used in criticality and reactor physics, with direct implications for safety margins and operational assessment.

This is precisely why modern Sensitivity and Uncertainty (S/U) analyses explicitly quantify how nuclear data uncertainties and biases map into uncertainties (and potential biases) on k_{eff} and related integral metrics.

When experimental information is scarce, incomplete, or limited in precision and trueness, evaluations must rely more heavily on theoretical models and systematics to fill gaps and enforce cross-channel and energy-range consistency. While this is unavoidable for comprehensive libraries, it introduces additional - and often hard-to-verify - sources of uncertainties, particularly in extrapolations beyond the measured domain. High-quality (in terms of precision and accuracy) measurements therefore play a dual role: they constraint where data exist and they calibrate and validate the models used to infer quantities where measurements are not feasible, thereby reducing extrapolation error and improving overall predictive performance. For these reasons, accurate and precise experimental data are essential not only to underpin evaluated libraries, but also to ensure the robustness of the entire simulation enterprise that depends on them. This logic is reflected operationally in international prioritisation mechanisms - such as the OECD-NEA High Priority Request List (HPRL) - which formalise where new measurements are most impactful for reducing uncertainties in application-relevant integral parameters.

1.3 The TAPIRO reactor

TAPIRO (**TA**ratura **PI**la **R**apida Potenza zer**O**)[17] is a low-power, fast spectrum research reactor operated by ENEA at the Casaccia Research Center near Rome (Figure 2). Commissioned in the early 1970s, it is primarily used as a fast-neutron source to support experimental programs on fast-reactor technology and related applications. The facility enables a wide range of activities, including validation of calculation tools and evaluated nuclear data, neutron propagation in different materials, irradiation tests for studying fast-neutron damage in materials and electronic components. It also serves an important educational role, by providing training opportunities for university courses and operators.

The reactor features a cylindrical core with a diameter of about 12 cm and a compa-

Figure 2: Reactor room of ENEA's research facility TAPIRO in Casaccia.

rable height. The fuel is a uranium–molybdenum alloy, with uranium highly enriched in ^{235}U. The core is made of two parts: the upper one is fixed, while the lower one is movable. Criticality is reached when the movable part of the core joins the fixed one.
Outside the core, a cylindrical natural-copper reflector is arranged in two layers (both about 70 cm in height): the inner layer has a diameter of 38.4 cm and the outer layer a diameter of 80 cm. The reflector improves neutron economy by returning part of the leakage neutrons back to the core. As an additional safety measure, the reactor is surrounded by a spherical biological shield made of borated concrete, about 1.75 m thick. As a fast-neutron source, TAPIRO is operated without a moderator. The cooling circuit was implemented using forced circulation of helium gas, which cools down the reactor without moderating the neutrons.
Several experimental irradiation channels are available, including two radial channels and one diametral channel on the mid-plane, complemented by a tangential channel [18]. The internal structure of the TAPIRO reactor is shown in Figure 3. Reactivity con-

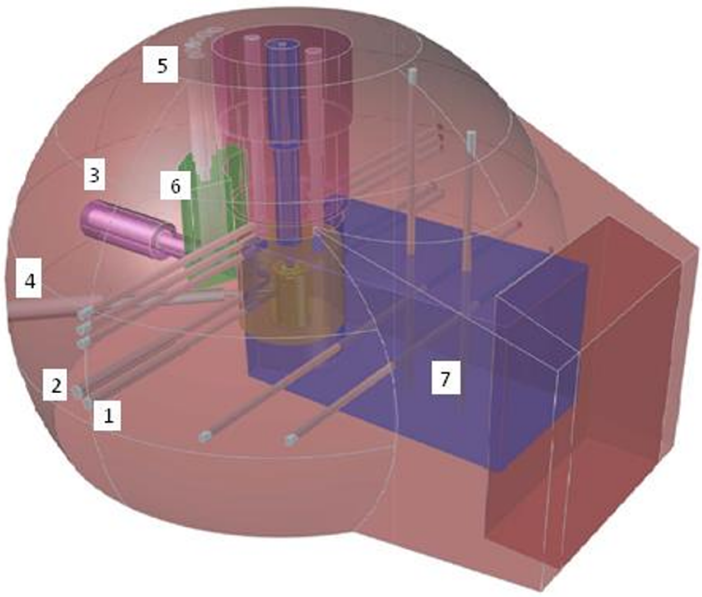

Figure 3: Internal structure of the TAPIRO reactor, with the experimental channels numbered: 1 - diametral channel, 2 - tangential channel, 3 - radial channel 1, 4 - radial channel 2, 5 - detector channels, 6 - paraffin, 7 - thermal column.

trol is achieved through copper control elements: two safety rods, two calibration rods and one regulation rod, all made of copper. Since these rods are made of a reflecting material, their effect is opposite to that of conventional absorber rods: inserting them increases the overall reflection towards the core, thus increasing k_{eff}, whereas withdrawing them increases leakage, thus reducing k_{eff}.
The reactor is designed to operate up to 5 kWth, corresponding to a maximum neutron flux of $4 \cdot 10^{12}$ neutrons $\cdot$ cm^{-2} $\cdot$ s^{-1} at the core centre.
The reactor provides a fast fission spectrum, peaked at 820 keV and with an average value around 1 MeV. In Figure 4, the neutron energy spectrum at the centre of the TAPIRO reactor is shown.

1.3.1 Relevance of copper data for TAPIRO

Copper is a key material in TAPIRO, as it constitutes both the reflector and the control elements. To quantify the impact of copper nuclear data on reactor criticality, sensitivity studies were performed with MCNP using the ENDF/B-VIII.0 nuclear data library [20]. In particular, the sensitivity of the effective multiplication factor k_{eff} was evaluated as a function of ^{63}Cu and ^{65}Cu neutron-induced total cross sections (Figure 5). Sensitivity values differ significantly from zero in a region between 10 keV and 10 MeV, with a peak at approximately 1 MeV. This matches exactly the energy spectrum of the TAPIRO

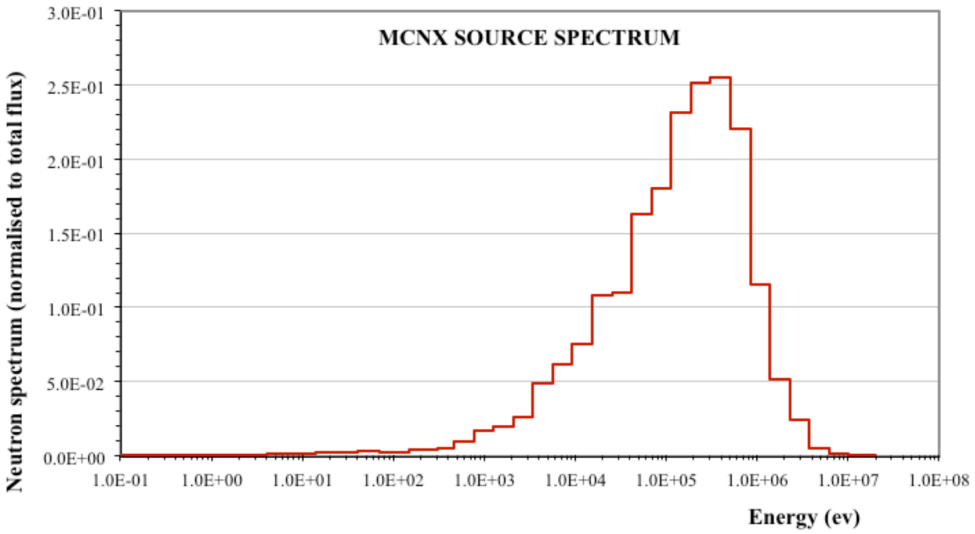

Figure 4: Neutron energy spectrum at the centre of the core of the TAPIRO reactor, peaked at 820 keV, estimated with MCNPX code [19].

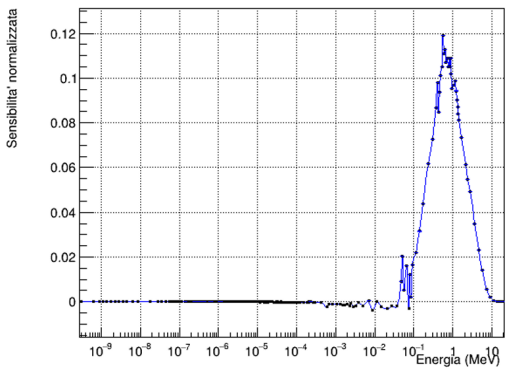

(a) Sensitivity for ^{63}Cu

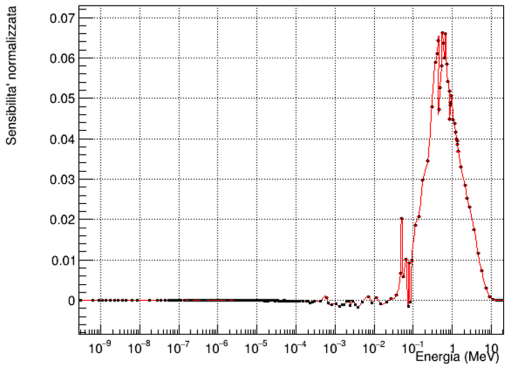

(b) Sensitivity for ^{65}Cu

Figure 5: Normalized sensitivity profiles of k_{eff} for (n,tot) cross sections of copper isotopes ^{63}Cu (a) and ^{65}Cu (b) [20].

reactor, shown in Figure 4, indicating that fast neutrons have the greatest influence on reactor criticality. Comparing the absolute values, it is possible to notice that the sensitivity is higher for ^{63}Cu, reflecting the isotopic composition of natural copper (69.15% of ^{63}Cu and 30.85% of ^{65}Cu). A sensitivity ranking was performed on several structural elements of the TAPIRO, and the results showed that, along with ^{235}U, copper cross sections are amongst the most important contributors on k_{eff}. These results highlight the importance of accurate cross section data of copper for the safety and control of the TAPIRO reactor, as well as for other systems which exploit the same technology, for research or energy production purposes.

1.4 State of the art of Cu(n,tot) cross sections

This section provides an overview of the state of the art of Cu(n,tot) cross sections, both in terms of experimental and evaluated data, highlighting the need for new, refined measurements.

Experimental data Total cross sections of copper isotopes, along with their resonance parameters, were measured in 1976 at Oak Ridge Electron Linear Accelerator (ORELA) [21]. The accelerator operates at a nominal energy of about 150 MeV, with electron bursts of width 5 ns and a repetition rate of 1000 pulses/s. Neutrons are produced with a peak intensity of 6 $\cdot 10^{18}$ neutrons/s in a small water-cooled laminated Ta target. The evaporation neutrons, with an average energy of 1 MeV, are moderated by a water moderator around the target. Shieldings, filters and collimators are employed to collimate and clean the neutron beam. The moderated neutrons travel down a flight path with detector stations located at 80 and 200 m from the target. The characteristics of the accelerator (pulse width, repetition rate, etc.), are chosen to optimize measurements in the neutron energy region from 3 to 500 keV. The copper measurements were performed at a flight distance of 78.2 m. The two samples of ^{63}Cu and ^{65}Cu, mounted in separate holders, were automatically cycled in and out of the beam. Neutron detection was carried out using a proton-recoil plastic scintillator coupled to a phototube for energies above 10 keV, and a Li-glass scintillator for lower energies. These data cover an energy range that spans from 50 eV to 150 keV.

Transmission experiments for (n,tot) copper cross section measurements were performed in 2013 at the neutron time-of-flight facility GELINA of the Joint Research Centre in Geel [22]. GELINA is a multi-user TOF facility, providing a white neutron spectrum from 10 meV to 20 MeV, with measurement stations located between 10 m and 400 m from the neutron production target. The electron linear accelerator delivers a pulsed electron beam with a maximum energy of 150 MeV and a repetition rate ranging from 50 Hz to 800 Hz. Neutrons are produced by photonuclear reactions in a mercury-cooled uranium target and moderated by two water-filled beryllium containers. By applying different neutron beam collimation conditions, experiments can use either a fast or a thermalized neutron spectrum. The transmission measurements were performed with a ^{nat}Cu sample and metallic samples enriched in ^{63}Cu and ^{65}Cu at the 50 m measurement station with the accelerator operating at 800 Hz. The neutron beam passing through the sample was detected by a Li-glass scintillator connected to a PMT. These measurements provided cross section data between 50 eV and 130 keV.

Copper cross sections were also measured at the Los Alamos National Laboratory in 1993 [23]. At the Weapons Neutron Research facility of the Los Alamos National Laboratory, neutrons are produced by spallation of the 800 MeV proton beam incident

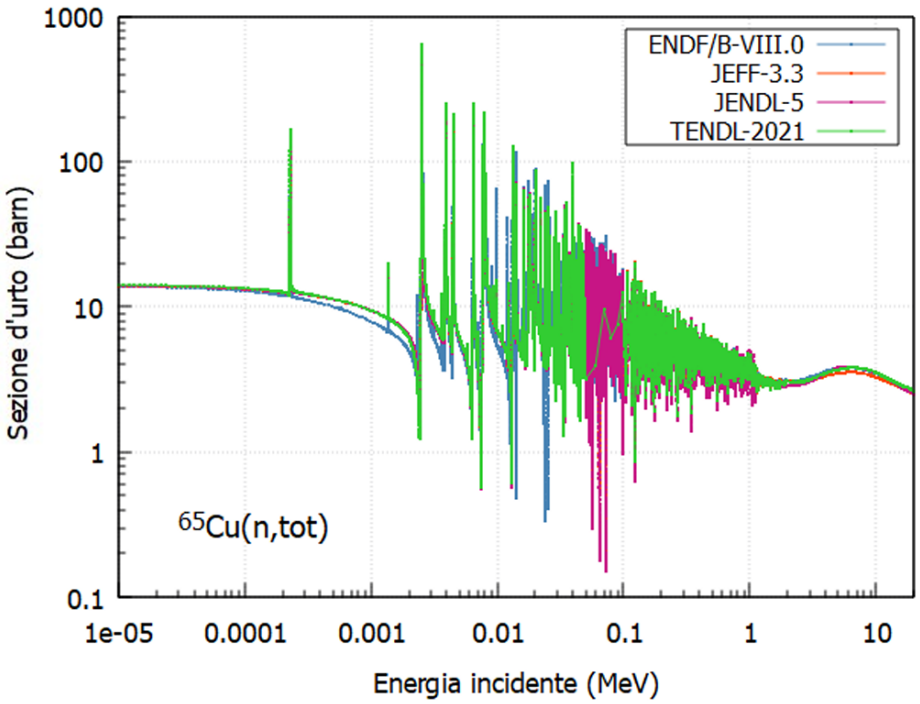

Figure 6: ^{65}Cu(n,tot) cross sections of several evaluated libraries, showing significant discrepancies [24].

on a thick, heavily shielded tungsten target. The resulting neutron spectrum is continuous and extends up to 600 MeV. A system of multiple collimators defines a narrow, well-controlled neutron beam and a long shutter collimator fixes the beam size at the sample position. Total cross sections were measured in a classic transmission experiment using a ^{nat}Cu sample. The transmitted neutrons were detected by means of a plastic scintillator detector coupled to two photomultiplier tubes.

Evaluated data Evaluated data of neutron-induced copper cross sections reported by some of the major nuclear libraries, namely ENDF/B-VIII.0, JEFF-3.3, JENDL-5.0 and TENDL-2021, were compared [24]. These libraries showed significant discrepancies for both ^{63}Cu and ^{65}Cu data. Figure 6 presents a plot of the total cross section for the isotope ^{65}Cu, from which it is possible to appreciate the discrepancies between data corresponding to the different libraries.

These studies showed that in the energy region within 50 and 100 keV, the considered libraries differ in the number of resonances that they report, while in the unresolved resonance region, their cross section values show discrepancies up to 30% [25].

As already described in Section 1.2, the accuracy of evaluated data is essential for

the applications, with even small biases potentially causing significant errors in the estimates of the integral parameters of a nuclear reactor. This is particularly true for the TAPIRO reactor, which shows a significant sensitivity to copper cross sections, as explained in Section 1.3.1.

1.5 The RAMEN experimental campaign

The inconsistencies found in the neutron-induced copper cross sections provided by major evaluated libraries, together with the limited experimental constraints available for several key reaction channels motivated the proposal of an experimental campaign aimed at refining copper nuclear data [26]. Given the neutronic relevance of copper for the TAPIRO reactor, the Italian National Agency for New Technologies, Energy and Sustainable Economic Development (ENEA), in collaboration with INFN, launched an experimental campaign named RAMEN within the Euratom-funded APRENDE project [27]. The RAMEN campaign is intented to improve copper evaluations by performing new experimental measurements at the CERN n_TOF facility [25], described in Chapter 2.

Since - as discussed in Section 1.3 - TAPIRO is a fast-spectrum reactor and therefore particularly sensitive to neutron energies in the kev-MeV region, the measurements were designed to strengthen the experimental basis precisely in the energy range most relevant to fast-spectrum applications.
Capture cross sections were measured in 2024 for both ^{63}Cu and ^{65}Cu, with data reduction currently in progress, while the measurement, by means of a transmission experiment, and analysis of total cross sections of ^{nat}Cu is presented in this thesis. A further objective of the campaign is to extend the experimental program to additional channels, in particular elastic and inelastic scattering, to provide a more comprehensive refinement of copper reaction data. However, measuring these reactions at n_TOF is particularly challenging and requires dedicated feasibility studies (including detector-development and background-rejection assessments). Preparatory tests, also involving complementary measurements, are currently underway to verify the measurements concept and to ultimately consolidate the experimental strategy.

2 The n_TOF facility

A wide range of research disciplines and applications rely on nuclear data. In particular, neutron-induced reaction cross sections are essential for the safety and criticality assessment of nuclear reactors, both the present-generation and the more innovative technologies, as Generation IV and fusion reactors, presented in Section 1.1.
Although nuclear theories and simulations can provide estimates of cross sections, experimental measurements are mandatory to reach the accuracy and reliability required by the aforementioned applications. For this reason, several facilities entirely devoted to the measurements of reactions induced by neutrons have been built around the world. Most of them exploit the Time-of-Flight technique (explained in detail in Section 2.2) to determine the energy dependence of neutron-induced cross sections. These facilities use different methods for neutron production and have flight path lengths ranging between less than one meter to 400m. Among these are n_TOF at CERN in Switzerland, GELINA at JRC-IRMM in Belgium, RPI and LANSCE in the USA and ANNRI at J-PARK in Japan [28].
The n_TOF facility, with its wide energy spectrum, high energy resolution and high instantaeous flux, represents one of the most active facilities in the field. A first overview is provided in the following Section (2.1).

2.1 Overview of the facility

The neutron Time-of-Flight facility [29], n_TOF, became operational at CERN in 2001, based on an idea by C. Rubbia. To cover the wide range of applications, at n_TOF the neutron energies span from few meV to several GeV. Thanks to this wide neutron energy range, along with a high instantaneous flux, the n_TOF facility has been one of the most active facilities since the beginning of its operations.
The neutron beam is generated by protons, coming from the CERN Proton Synchrotron, that impinge on a lead target, inducing spallation reactions (more details are provided in Section 2.3). A scheme of the CERN accelerator complex is presented in Figure 7. The Proton Synchrotron (PS) receives protons from the BOOSTER, accelerates them to 20 GeV/c, and delivers them to n_TOF, to the East Area, and to the Super Proton Synchrotron (SPS), to be further accelerated for injection in the LHC. Since 2025, the protons that are directly sent to n_TOF from the PS are grouped in bunches of $8.5 \cdot 10^{12}$ protons, called *dedicated*. Beams of lower intensity, on average $3.5 \cdot 10^{12}$ protons per bunch, are also sent the facility. To distinguish the two, they are referred to as high and low intensity dedicated bunches. Some of the protons that reach the East Area are sent to the n_TOF facility. These are called *parasitic* bunches and have an average intensity of $5 \cdot 10^{12}$ protons per bunch. The average repetition rate between bunches is 0.25 Hz, and for each bunch, the protons are concentrated in a time interval of 7 ns (rms).

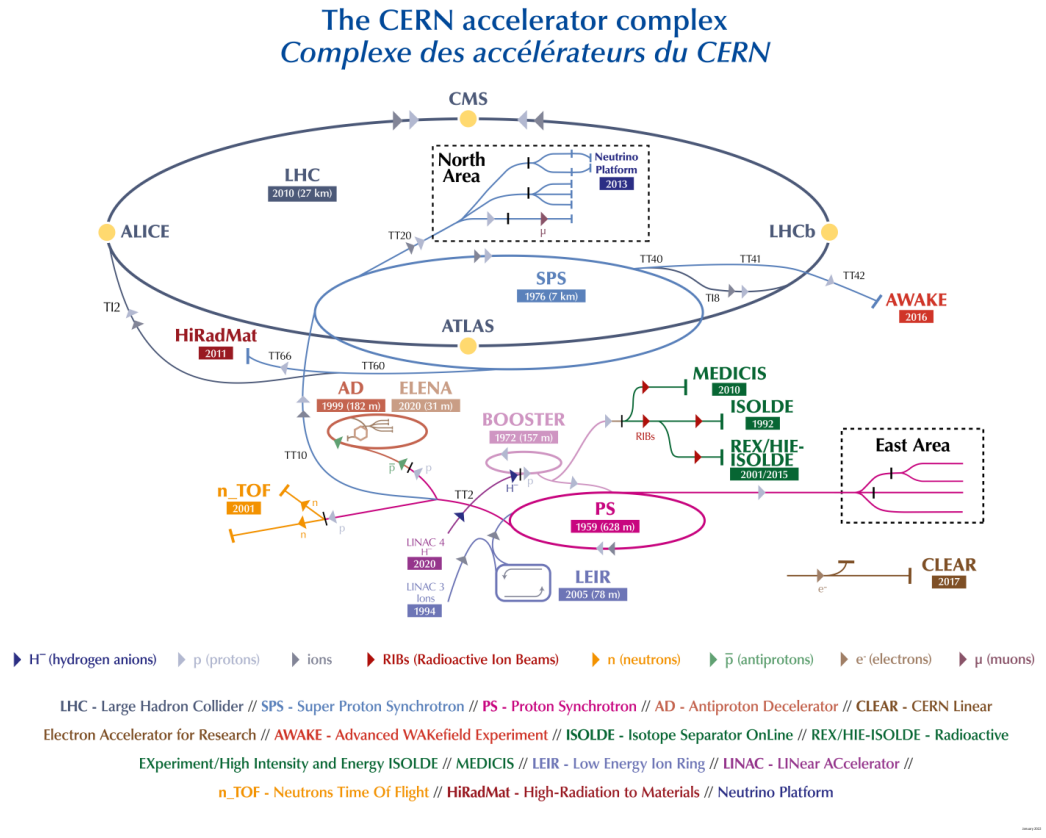

Figure 7: The CERN accelerator complex [30].

The position and profile of the proton pulses sent to the facility are provided by a SEM-Grid placed in front of the lead spallation target. Furthermore, the intensity is monitored before impact on the target by a detector called PKUP. It is a Wall Current Monitor and provides a signal proportional to the proton beam current. It is used to directly monitor the intensity, the effective delivery of protons by the PS and for timing purposes.
Neutrons produced by spallation are then moderated, to further enlarge the neutron energy spectrum, and driven to the experimental areas. Two vacuum tubes, equipped with collimators and sweeping magnets, ensure the selection of neutrons among other particles produced during spallation, and carry the neutron beam to the first two experimental areas. EAR1 is placed at 182.5 m from the spallation target, along the horizontal beam line, while EAR2 is positioned 18.2 m above it. In the recent years, a third experimental area, NEAR, was built at just 3 m from the target.
From the measurement of the arrival time of the neutrons at the experimental areas, their energy can be deduced, according to the time-of-flight technique, described in

section 2.2. Further details about the spallation target and the experimental areas can be found respectively in sections 2.3 and 2.4. Section 2.5 presents an overview on neutron flux detectors at n_TOF, which are crucial for transmission measurements.

2.2 The time of flight method

The Time-of-Flight method exploits the fact that the flight path of the neutrons (L) is fixed. It is then possible to extract the time a neutron has traveled as the difference between a start signal, corresponding to the time of its production, and a stop signal, corresponding to the moment of its interaction with the detection system. More details about how the TOF is measured will be given in the next Section (2.3). By knowing L and TOF, the velocity of the neutron, and therefore its kinetic energy, can be computed. The velocity is defined as follows:

$$v = \frac{L}{TOF} \tag{1}$$

and it is used to compute the Lorentz factor:

$$\gamma = \sqrt{\frac{1}{1 - v^2/c^2}} \tag{2}$$

which enters into the expression of the kinetic energy:

$$E_n = E - mc^2 = \sqrt{p^2c^2 + m^2c^4} - mc^2 = mc^2(\gamma - 1) \tag{3}$$

In the non-relativistic regime, the classical formula can be used:

$$E_n = \frac{1}{2}mv^2 \tag{4}$$

It is possible to evaluate also the energy resolution, as follows:

$$\frac{\Delta E_n}{E_n} = \gamma(\gamma+1)\frac{\Delta v}{v} = \gamma(\gamma+1)\sqrt{\left(\frac{\Delta TOF}{TOF}\right)^2 + \left(\frac{\Delta L}{L}\right)^2} \tag{5}$$

The energy resolution is an important quantity because, in the broad energy spectrum produced at n_TOF, the cross section exhibits many resonances. These structures, which are not predictable beforehand and must be evaluated experimentally for each isotope, are very close together, with the distance between consecutive resonances decreasing with neutron energy. Therefore, to accurately resolve these structures, it is essential to conduct experiments with sufficient energy resolution.
The energy resolution improves for longer flight paths (large L and TOF). Therefore, the choice of the experimental area, which determines the flight path length, has an impact on the best resolution achievable.

2.3 Neutron beam production

The neutron beam at the n_TOF facility is produced through spallation reactions induced by protons impinging on a lead target. As previously explained in Section 2.1, the proton pulses have intensities of $8.5 \cdot 10^{12}$ and $3.5 \cdot 10^{12}$ respectively for high and low intensity dedicated bunches, and $5 \cdot 10^{12}$ for parasitic bunches. The maximum repetition rate of the delivered proton pulses is 0.8 Hz while the time width of each pulse is 7 ns (rms), allowing for excellent energy resolution of the produced neutron beam, even for the GeV neutron energy region [31]. On average, 300 neutrons are produced through spallation reactions per incident proton.

2.3.1 Spallation reaction

Spallation is an inelastic nuclear reaction that occurs when a high-energy particle hits a target nucleus, causing the emission of many neutrons. This reaction is a sequential process: the incident particle is absorbed by the target nucleus, which first reaches an excited state and then undergoes an intranuclear cascade. Then, an internuclear cascade happens, where high-energy particles, including neutrons, are expelled and absorbed by other nuclei. Finally, the various target nuclei undergo "evaporation", a process that consists of their de-excitation, followed by the emission of several lower-energy neutrons and various types of nucleons, photons, and neutrinos.
During the spallation process, many high-energy photons are emitted, most of which come from the decay of pions produced in the cascade. These photons, together with other ultrarelativistic particles, constitute the fast component of the so-called γ-flash. There is also a slow component, due to neutrons undergoing radiative capture reactions in the lead and moderation layers.
The γ-flash is seen by detectors in the experimental areas before any other signal, and it obscures data acquisition for its entire duration, which can reach hundreds of nanoseconds. Despite this dead-time effect, the γ-flash provides a useful method for time calibration. By correcting its time, t_γ, for L/c, which is the time taken for the photons to reach the detector, it is possible to know the time when spallation reactions occurred. This corresponds to the instant of neutron production, which is the starting time of the TOF signal. The stop time is the instant when the signals are detected, so the TOF can be computed as

$$TOF = t_{stop} - t_{start} = t_{signal} - t_\gamma + L/c \tag{6}$$

2.3.2 Spallation target

The n_TOF facility employs a third-generation spallation target [32], developed on the basis of the operational experience obtained from the first two designs. The first-generation target operated from 2000 to 2004 and the second from 2008 to the end of 2018. Even though the second target included many upgrades compared with the first one, both

were cooled by water in direct contact with pure lead, which caused corrosion and contamination problems. Moreover, both targets were not optimized for vertical beam production, since the second experimental area, EAR2, was built only in 2014.
The third-generation target [33] was installed during the Long Shutdown 2 and started operations in 2021. Its assembly is shown, in exploded view, in figure 8. The core is housed inside a stainless steel vessel and is made of six lead slices, which are cooled by gaseous nitrogen and supported by precisely machined anticreep plates. The lead slices are 5 cm thick, with the exception of the slice close to the EAR1 moderator, which is 15 cm thick. The anticreep plates are made from aluminum alloy and include the channels through which the cooling fluid flows. The cooling gas is distributed through two main arteries inside a cradle made from aluminum alloy, which supports the lead core from below. Connected to the vessel, two moderator containers, made from aluminum alloy and connected to independent water circuits, are positioned on the path of the neutrons directed to the two experimental areas.
The new target has several advantages in terms of radioprotection. The nitrogen cooling system eliminates the corrosion issues caused by direct contact between water and lead in earlier designs. Previously, spallation products, including α and γ emitters, could migrate into the cooling water, creating radiological risks. By using a nitrogen-based cooling circuit, the release of lead spallation products is greatly reduced, enhancing radiological safety during maintenance.
Along with the target, the target shielding was also upgraded, with a thicker and mobile version that reduces air activation in the target area and allowed the installation of the NEAR station close to the spallation target.

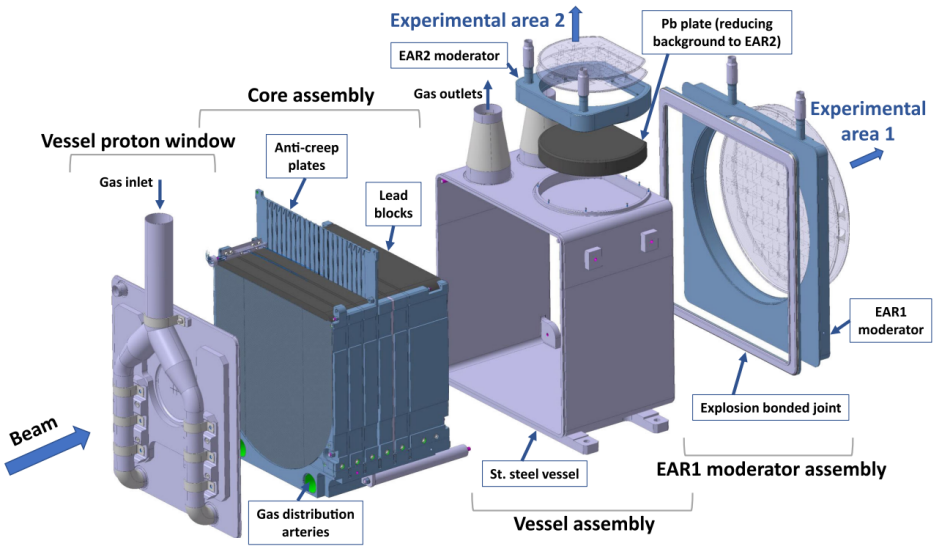

Figure 8: 3D model of the third-generation lead spallation target currently employed at the n_TOF facility [33].

2.4 Experimental areas

The n_TOF facility features three experimental areas, with different flight paths and therefore different neutron flux and energy resolution. The experimental area is chosen according to the needs of each experimental campaign. EAR1 and EAR2 are mostly used for cross section measurements exploiting the TOF technique, while NEAR is best suited for activation measurements and radiation-damage studies. Figure 9 shows an overview of the three experimental areas, along with their distinctive features, which will be better explained in the next sections.

2.4.1 EAR1

The EAR1 experimental area was the first one built, in 2001, when the n_TOF facility began operations. It is placed at a horizontal distance of 182.3 m from the spallation target and is 7.9 m long [34]. The beamline is tilted by 10° with respect to the incoming primary proton beam, in order to reduce the background of charged particles and photons that consitute the γ-flash. A sketch of the evacuated beamline is presented in figure 10. A sweeping magnet, 2 m long, deflects the in-beam charged particles and two collimators shape the neutron beam. The second collimator can be changed to accommodate the needs of different types of experiments: a collimator with a diameter of 18 mm is used typically for measurements of the radiative capture channel of neutron-induced reactions, while a collimator with a 80 mm diameter is used for measurements of the fission channel. Inside the experimental area, several detectors can

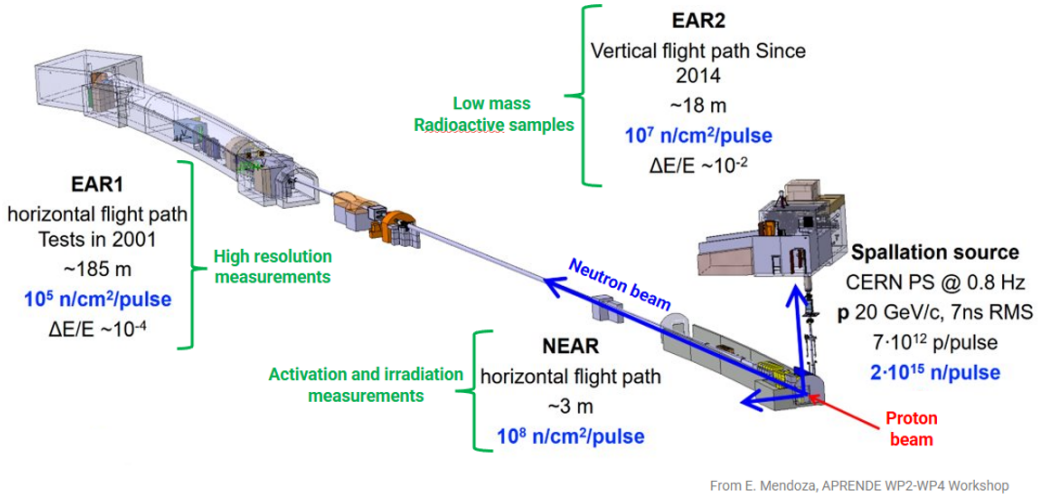

Figure 9: Overview of the three experimental areas at the n_TOF facility. Key characteristics of the proton beam before impinging on the spallation target are reported, together with the neutron flux produced by spallation. For each experimental area, the corresponding flight path, best energy resolution, and neutron flux are indicated.

be mounted. They are chosen according to the reactions under study. Typically, liquid (C_6D_6) and solid (BaF_2) detectors are used to measure the γ rays following radiative capture reactions, while gas (MicroMegas) and solid-state detectors (silicon, diamond) are used for (n,charged-particle) reactions. Fission experiments are usually performed with gas detectors (MicroMegas, PPAC).

The neutron flux in EAR1 is of the order of 10^6 neutrons/bunch, the lowest among the three areas, due to the longer flight path. The energy resolution, on the other hand, is the best one, with a value of $\Delta E/E \sim 10^{-4}$ at 1 eV. For this reason, EAR1 is best suited for high-resolution measurements, particularly in the resonance region.

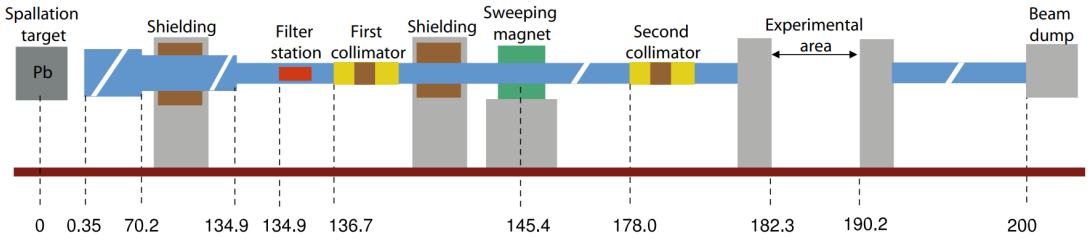

Figure 10: Layout of the n_TOF-EAR1 neutron beamline, from the spallation target to the beam dump [34]. Indications of the distances are given in meters.

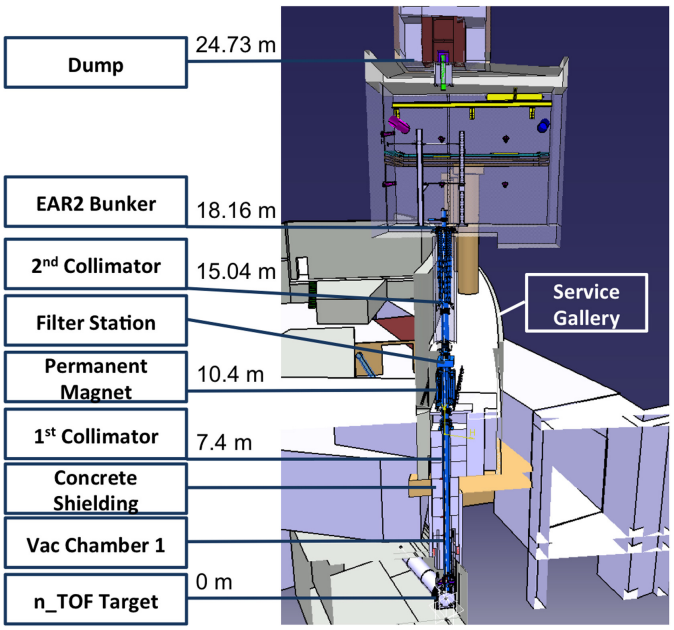

Figure 11: n_TOF-EAR2 beamline, with the main elements labeled and distances relative to the spallation target indicated [35].

Since neutrons in this area can be detected up to kinetic energies of few GeV, EAR1 is also used to extend measurements of neutron-induced reaction cross sections to high neutron energies.

2.4.2 EAR2

The second experimental area, EAR2, was constructed in 2014. It is located on a vertical flight path, at a distance of 20 m from the spallation target. A sketch of the beamline is presented in figure 11. Analogously to EAR1, permanent magnets and collimators are used to shape the neutron beam. The experimental area begins at a distance of 18.16 m from the spallation target and the beam dump is at 24.73 m. Since the upgrade of the spallation target in 2021, the quality of the neutron beam at EAR2 has improved significantly, in terms of flux, energy resolution, and beam profile. Now, the neutron flux at EAR2 is about 10^7 neutrons/bunch, while the energy resolution can reach $\Delta E/E \sim 10^{-3}$ at 1 eV. These features make EAR2 suitable for measurements of neutron-induced reactions on very thin samples, radioactive isotopes with short half-life and reactions with low cross sections [36].

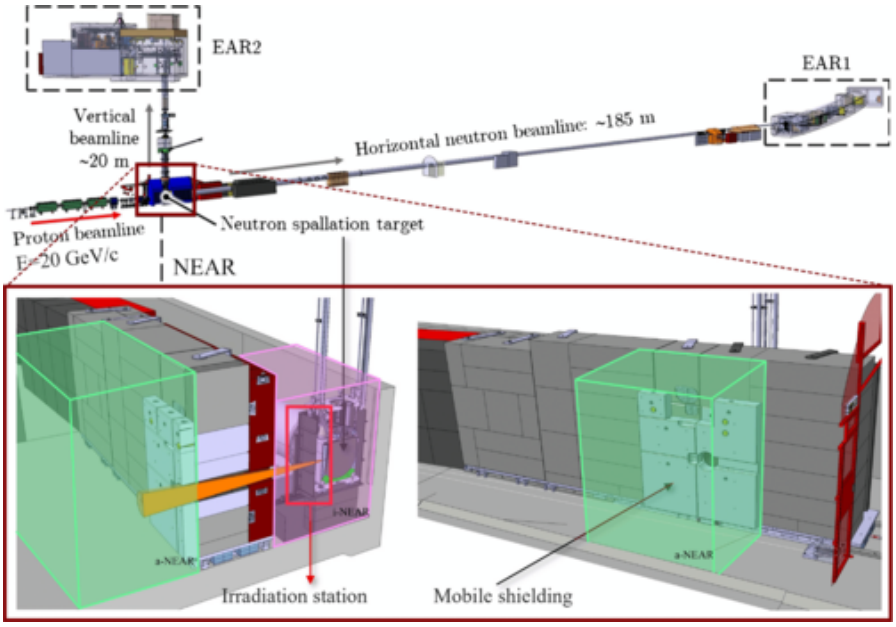

Figure 12: Top image: scheme of the NEAR station location at n_TOF [37]. Bottom image: different views of the NEAR area. The activation area (a-NEAR) is outlined by the green volume, while the irradiation area (i-NEAR) corresponds to the pink volume.

2.4.3 NEAR

The upgrade of the spallation target during the Long Shutdown 2 allowed the installation of a third experimental hall close to the target, called NEAR. The area became operational in July 2021 and a scheme of its location at n_TOF and of its structure is presented in figure 12. The mobile target shielding separates the NEAR Irradiation area (i-NEAR), which includes the target and where a station is installed mainly focused on the irradiation of materials and electronics. Outside the shielding there is the NEAR Activation area (a-NEAR), which includes a neutron collimator and the main position devoted to cross section measurements by the activation technique [37]. The neutron beam reaches the a-NEAR through a hole in the shielding wall and is optimized thanks to a collimation system. Due to the close proximity with the target, an extremely high neutron flux, as well as a significant flux of γ rays and charged particles, reaches the NEAR station. The high flux makes this experimental area suitable for measurements on very small samples and extremely short-lived radioactive isotopes, but also allows to acquire data on radiation damage in a neutron-dominated environment. The extreme radiation conditions, however, present some technical challenges in terms of experimental detection. The TOF technique is less effective due to the short distance from the target and the high radiations complicate the use of standard detectors and electronics. To face these challenges, some offline techniques have been developed. An

example is Multi-foil Activation Measurements, where small or radioactive samples are irradiated at the NEAR station and then analysed offline with a High Purity Germanium detector (HPGe).
Furthermore, with the use of filters, i.e. B_4C, it is possible to shape the neutron spectrum and make its energy distribution as close as possible to a Maxwellian distribution. This technique would simulate the neutron flux distribution present in the stars and would allow for integral measurements relevant for astrophysics, especially when the cross section is too low or the material available is of the order of mg.
Thanks to all these features, in addition to the fact that it can operate in parallel with EAR1 and EAR2, the NEAR station contributes to the expansion of the experimental capabilities of the n_TOF facility.

2.5 Flux detectors

Detectors capable of measuring the neutron flux are fundamental for carrying out transmission measurements. At n_TOF, several types of flux detectors are employed [38], and the choice of which one to use depends on the specific goals and requirements of each experiment.
The neutron flux is measured by exploiting some neutron-converting reactions, namely ^{6}Li(n,α), ^{10}B(n,α) and ^{235}U(n,f). These reactions are characterized by very high accuracy cross sections in some energy regions, where they are considered standards. By selecting and analysing the products of these reactions, the neutron flux can be measured in each case.
One of the detectors used at n_TOF is SiMon (Silicon Monitor device) [36], a solid state detection system equipped with a ^{6}Li converter. The detector consists of a Mylar foil, with a deposit of ^{6}LiF, centered in the beam and surrounded by an array of four silicon detectors outside the beam in the forward direction. By recording the tritons and alpha particles emitted in ^{6}Li(n,α) reactions, this system is able to monitor the neutron flux, and is particularly suitable for capture cross section measurements.
Another neutron flux detector employed at n_TOF is MGAS (Micromegas gas detector), which exploits ^{10}B and ^{235}U as converters. These elements are deposited on cathodes and mounted inside an aluminum chamber, with Kapton windows, filled with a gas circulating at atmospheric pressure. This detector, characterized by low noise, high radiation resistance and low mass, has been used at n_TOF for measuring the total neutron flux and the spatial beam profile, as well as for neutron-induced fission cross section measurements.
A third detection system is a set of Parallel Plate Avalanche Counters (PPAC) [39]. The PPAC are equipped with a ^{235}U deposit on aluminum backing. Each consists of a central anode, flanked by two position-sensitive cathodes, and is filled with a low-pressure gas. The PPACs are insensitive to γ-radiation and have a very fast response. They have been used to measure the n_TOF neutron flux and beam profile with high accuracy.

Finally, to measure the neutron flux, a Low Mass Fission Chamber (LMFC) from the Physikalisch-Technische Bundesanstalt research institute can be used [40]. It is an ionization chamber equipped with six ^{235}U deposits on aluminum electrodes. This system is very well characterized in terms of detection efficiency and uniformity of the fissile deposit and is perfectly suited for the measurement of both absolute neutron flux and its energy dependence in the energy range between 0.15 and 200 MeV, where ^{235}U(n,f) cross section is considered a standard. It has also been extensively used for cross section measurements. This detector was employed for the experiment that is presented in this thesis and is described in greater detail in section 3.3.
Overall, these detectors provide high-resolution measurements of the neutron flux, which are essential for transmission experiments, aimed at measuring total cross sections, as explained in the following section (3.1).

3 The transmission experiment of ^{nat}Cu at n_TOF

At the n_TOF facility, several types of experiments are performed. Among these are capture measurements, which aim to extract (n,γ) cross sections by measuring the γ cascade generated by radiative capture reactions, fission measurements, dedicated to the study of neutron-induced fission reactions, and charged particles reaction studies. Only recently, transmission measurements with the goal of determining total cross sections have been introduced at n_TOF, with the first tests performed in 2023. The ^{nat}Cu experiment presented in this thesis represents one of the first transmission campaigns at n_TOF.

The principles of transmission measurements are discussed in Section 3.1. Section 3.2 describes the experimental setup used during the ^{nat}Cu measurement, while Section 3.3 provides a detailed description of the detector employed. Finally, an overview of the measurement campaign and additional relevant details are provided in Section 3.4.

3.1 Principles of transmission measurements for total cross section determination

Transmission experiments are performed with the goal of extracting neutron-induced total cross sections. These measurements are based on the comparison of the neutron flux incident on a sample with the flux transmitted through it.
Figure 13 shows a sketch of a transmission experiment, with the neutron beam impinging on a sample.
Defining as J_{in} the incident neutron flux, the flux transmitted through the sample is given by

$$J_{out} = J_{in} e^{-n\sigma_{tot}} \tag{7}$$

where n is the areal density of the sample, measured in atoms/barn, and σ_{tot} is the total reaction cross section, in barn.
The transmission factor - also referred to as transmission - quantifying the fraction of particles passing through the sample without interacting, is defined as

$$T = \frac{J_{out}}{J_{in}} = e^{-n\sigma_{tot}} \tag{8}$$

By definition, T only takes values between 0 and 1, with T=0 corresponding to the complete absorption of the incident neutrons and T=1 indicating that all neutrons passed through the sample without interacting. The total cross section can then be extracted

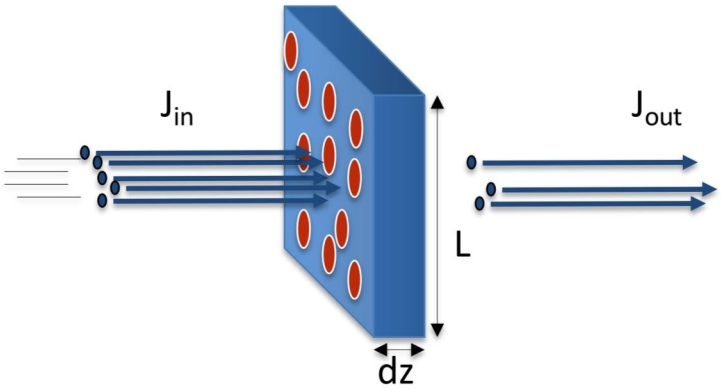

Figure 13: Sketch of a transmission experiment [41]. J_{in} and J_{out} are the incident and outgoing neutron flux, respectively. At the centre, a representation of the sample made of the material under study is shown.

by inverting the former relation, obtaining

$$\sigma_{tot} = -\frac{\ln T}{n} \tag{9}$$

The incident neutron flux can be experimentally determined by performing measurements without the sample in the beam. The transmission factor is thus computed as the ratio between the number of counts measured with the sample in the beam and the number of counts measured without the sample. Any systematics linked with the experimental setup should cancel out when computing T, since, assuming a stability over time, the setup is the same for the two configurations, with the only difference being the presence of the sample.

The neutron flux is measured by means of flux detectors, described in Section 2.5, which are characterized by a detection efficiency that determines their capability of detecting the interactions over the whole incident neutron kinetic energy range. The quantity that they actually measure is thus the neutron flux (either incident or transmitted) multiplied by the detection efficiency ($J \cdot \epsilon$). If the efficiency of the detector remains constant throughout the entire experimental campaign, hence it is the same for measurements performed with and without the sample, it should cancel out when computing the transmission ratio. To ensure the reliability of transmission measurements, it is therefore crucial to monitor the stability of the detectors over time.

3.2 Experimental setup

The n+^{nat}Cu experiment was performed with the goal of measuring total cross sections, therefore it consisted of a transmission measurement, as explained in the previous sec-

tion (3.1). It was carried out in EAR1, the experimental area providing the highest energy resolution among the three available at n_TOF, as decribed in Section 2.4.1.
A copper sample was placed on the transmission line, just downstream of the capture collimator, as shown in Figure 14. It consisted of a disk made of natural copper, composed of 69.15% of ^{63}Cu and of 30.85% of ^{65}Cu, with a thickness of 6 mm and a diameter of 3 cm. At this position, the neutron beam has a width of 1.8 cm, ensuring that it is fully intercepted by the sample.
Measurements were performed both with the copper sample in the beam ("Sample-

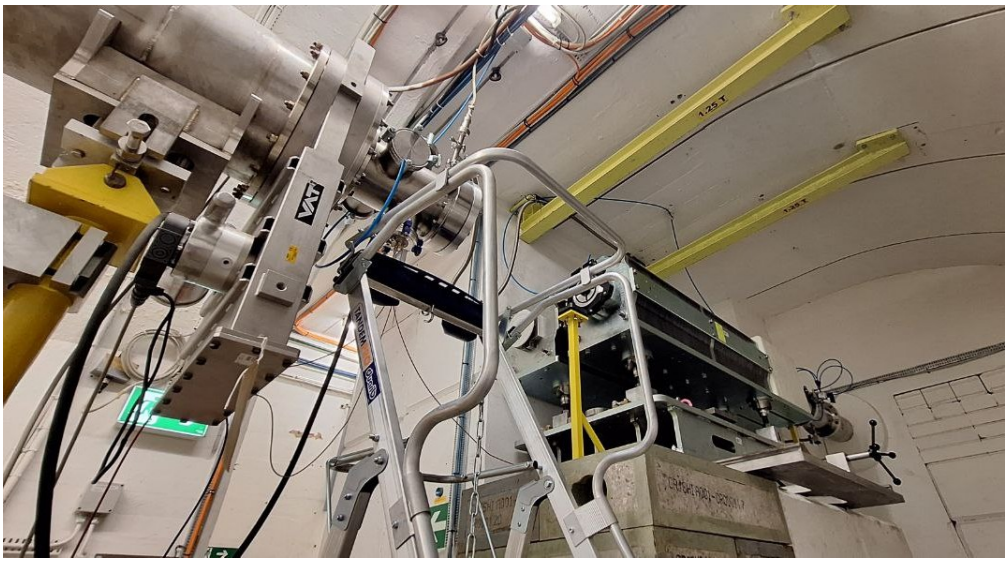

Figure 14: Trasmission station of EAR1. The capture collimator is visible in the left side of the figure, while the sample holder is located on the right.

in") and without it ("Sample-out"), as shown in Figure 15. The two configurations were alternated on a weekly basis, for a total of four weeks.

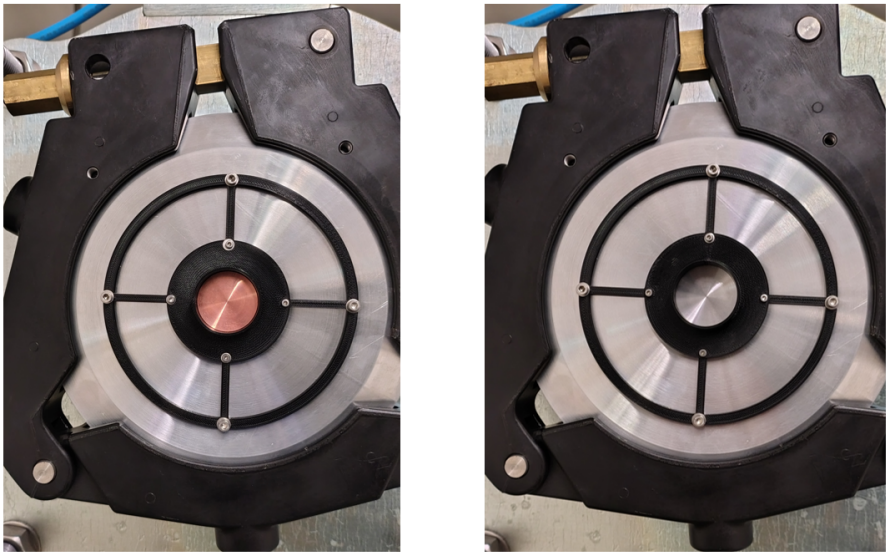

Figure 15: Sample holder on the transmission line. In the left image, the copper sample is present (”Sample-in” configuration), while in the right picture no sample is present (”Sample-out” configuration).

On the other side of the wall, inside the experimental area EAR1, a low mass fission camber was installed. This detector was used to record the neutron-induced signals and is described in detail in the following section (3.3).

3.3 Low mass fission chamber

The detector employed in the n+^{nat}Cu experiment is a Low Mass Fission Chamber (LMFC) developed by the Physikalisch-Technische Bundesanstalt (PTB) institute [40], already introduced in Section 2.5. It consists of a parallel-plate fission ionisation chamber mounted in a low mass setup with thin Kapton windows, designed to minimise neutron interactions. Figure 16 shows the external view of the LMFC, where the Kapton entrance window and the connector housings are visible, while Figure 17 presents the internal structure of the detector.

The LMFC contains a stack of six ^{235}U fissile samples, with a diameter of 42 mm each. The samples are deposited on aluminum backings with a thickness of 30 μm, which is significantly larger than the range of fission fragments in aluminum. This ensures that the fragments are fully stopped inside the backing and do not contaminate adjacent layers. Pairs of samples were mounted back-to-back in aluminum holder rings connected to ground potential, so that the samples act as cathodes. The anodes facing the samples consist of 20 μm aluminum foils glued to 1 mm thick rings made of fiber-reinforced plastic material (G10). The anode foils have a yellow backside, which is visible in Figure

Figure 16: LMFC outiside top view. It is possible to observe the Kapton window and the space for the connectors.

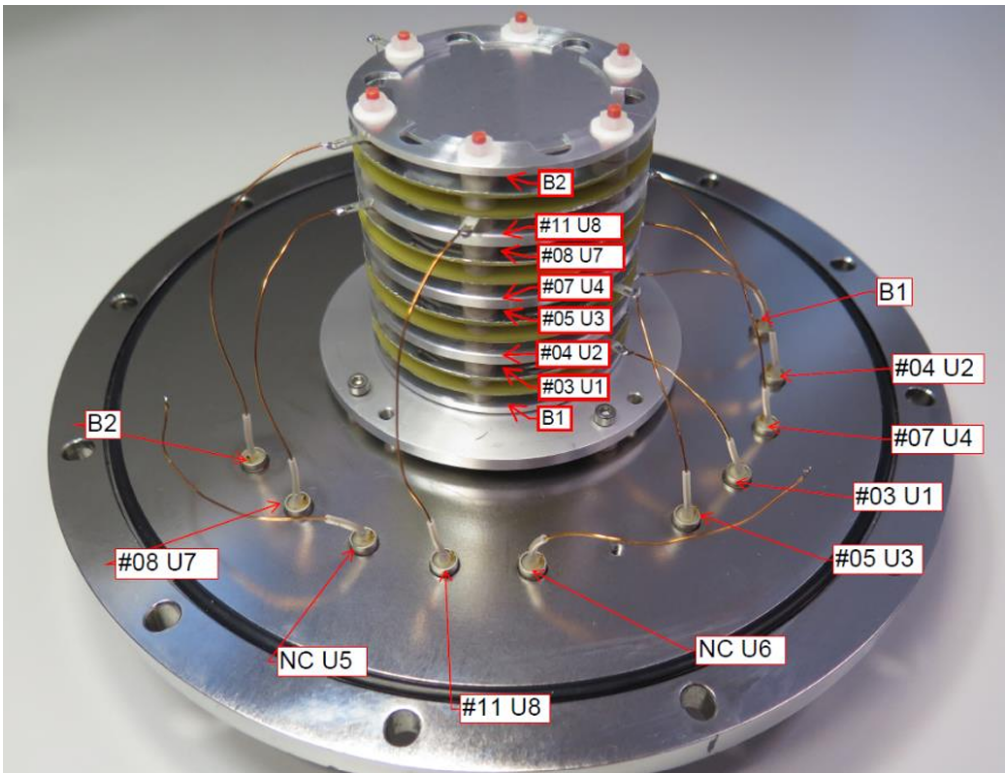

Figure 17: LMFC inside view. The labels refer to the different channels, with 'U' representings channels connected to Uranium samples and 'B' being the empty channels.

17, and their thickness is sufficient to stop fission fragments emitted from the adjacent fissile layer. The cathode and anode foils are held at a distance of 5 mm by six PEEK

spacers. Three stacks containing two cathodes and two anodes each were assembled and placed on top of each other, with spacers between adjacent anodes such that the distance between the anode foils is 3 mm. The six ^{235}U layers are labeled U1, U2, U3, U4, U7, U8 in Figure 17.
Below and above the stack, two additional cathodes equipped with blank samples (without the Uranium deposit) were mounted, together with their corresponding anodes. These channels, labeled B1 and B2 in the picture, are intended for background measurements. Only one of them (B1) was connected and registered data during the transmission measurement.
The chamber was sealed and operated in continuous flow mode at low ambient pressure, regulated by the gas flow system using Ar/CF_4 (10% vol).
The LMFC was placed in EAR1 and the electronics connections were made. Each channel was first connected to a Canberra preamplifier and then to an ORTEC amplifier, with a voltage supply of +230V. Figure 18 shows the fission chamber in the final setup inside EAR1, with the amplifiers and pre-amplifiers connected.

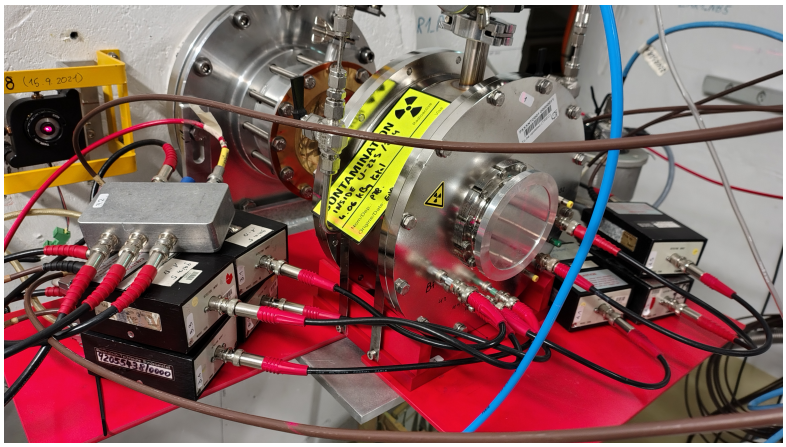

Figure 18: LMFC installed in EAR 1 for the n+^{nat}Cu experiment.

Figure 19 shows a typical fission fragment signal detected by the LMFC.

The TOF assigned to the events is defined using the constant fraction method, and in this case is equal to 911535 ns. The risetime, defined as the time taken for the signal to go from 10% to 90% of its maximum amplitude, is 53 ns. The full width at half maximum (FWHM) is 110 ns. The amplitude of the signal is measured in channels, where one channel corresponds to 0.0742 mV. The signal in Figure 19 has an amplitude of 36002 channels, which corresponds to 2671.4 mV.

In this way, many information about the events were registered by the LMFC. The most relevant quantities for the analysis are the time-of-flight and the signal amplitude. For the n+^{nat}Cu experiment, a detailed analysis of these two quantities was performed,

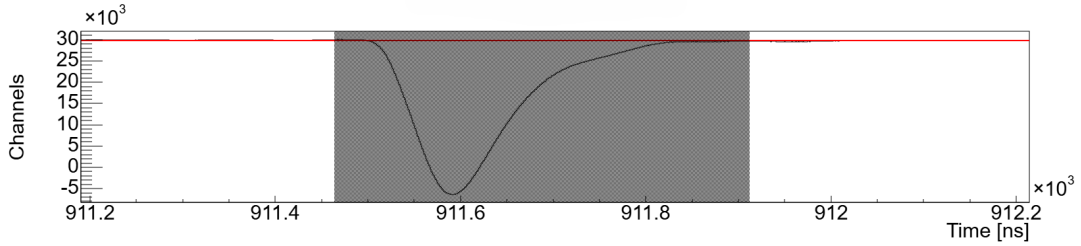

Figure 19: Raw signal induced by a fission fragment, detected by channel 7 of the LMFC.

and is described in Sections 4.2 and 4.3.

It is worth mentioning that the six channels of the fission chamber were read out separately, which allowed their independent analysis.

3.4 Measurement campaign

The n+^{nat}Cu transmission measurement was performed at n_TOF between May and June 2025. As already mentioned in Section 3.2, the experimental configuration was alternated weekly between Sample-in and Sample-out. The exact dates of each measurement week, together with the corresponding configuration and total number of protons, are reported in Table 2.

The experiment was carried out with a total of $3.66 \cdot 10^{18}$ protons, out of which

Week 1 21/05 - 28/05	Week 2 28/05 - 04/06	Week 3 04/06 - 11/06	Week 4 11/06 - 17/06
Sample-in	Sample-out	Sample-in	Sample-out
$8.55 \cdot 10^{17}$ p	$8.37 \cdot 10^{17}$ p	$1.13 \cdot 10^{18}$ p	$8.36 \cdot 10^{17}$ p

Table 2: n+^{nat}Cu measurement timeline. The exact dates of the 4 weeks of measurement are reported, along with the corresponding configuration and number of protons.

$1.99 \cdot 10^{18}$ were measured in the Sample-in and $1.67 \cdot 10^{18}$ in the Sample-out configuration. Table 3 reports how many of the total protons came from dedicated pulses and how many from parasitic.

Total protons	$3.66 \cdot 10^{18}$
Dedicated protons	$2.38 \cdot 10^{18}$
Parasitic protons	$1.28 \cdot 10^{18}$

Table 3: Total number of protons of the n+^{nat}Cu measurement campaign and their distinction between dedicated and parasitic.

The data were acquired in multiple runs. Each data acquisition window was stopped once $2 \cdot 10^{16}$ protons had been delivered, corresponding to approximately 3 hours of continuous data taking. Data from different runs were then summed together for a combined analysis.

The following chapter describes the analysis of the data collected during the n+natCu transmission experiment.

4 Data Analysis

This chapter focuses on the analysis of data of the n+^{nat}Cu experiment at n_TOF.

The pulses registered by the Low Mass Fission Chamber detector were identified and processed and, for each acquisition channel, the amplitude and TOF information were registered.

Since the six channels of the detector were read out separately, an independent analysis of each channel was performed. Another distinction consistently applied throughout the data analysis is between data corresponding to Sample-in runs and that corresponding to Sample-out. These datasets are fundamentally different and therefore have been analysed separately.

The first section (4.1) of this chapter describes the optimization of the Pulse Shape Analysis routine, which concerns the recognition of pulses from the raw signals, before their processing. Then, a detailed analysis of the amplitude spectra was carried out, as described in section 4.2. This study involved the determination of amplitude thresholds to discriminate fission fragment events from background events and the assessment of the stability and the efficiency of the detector. Afterwards, time-of-flight spectra were analysed (Section 4.3) and TOF and transmission histograms were built. Finally, applying the selection conditions and calibration values established by the aforementioned analyses, the cross section as function of neutron energy was extracted, and is described in Section 4.4.

4.1 Pulse Shape Analysis optimization

Data are acquired by sampling and storing the complete analog waveform of the detector signals for each neutron pulse, in the form of raw data files. Once stored in digital format, the electronic signals are accessible for offline analysis in order to obtain information on the flight time and pulse height. Raw signals registered by the detectors at n_TOF undergo a Pulse Shape Analysis (PSA) procedure which has the purpose of selecting only the pulses corresponding to actual event signals.

Figure 20 presents a typical waveform registered by channel 7 of the LMFC. The red horizontal line represents the baseline, which is the reference level for the determination of signal properties, such as the pulse amplitude. The first pulse visible in the waveform corresponds to the γ-flash, which is the first signal that reaches the detector, at approximately 11.2 x 10^3 ns after the opening of the acquisition window. The yellow vertical line marks the identification of the γ-flash by the PSA algorithm. The grey bands indicate time intervals in which the PSA routine has identified valid signals. Only pulses recognized by the algorithm are selected to be later processed, while all other parts of the waveform are discarded.

The criteria by which the PSA algorithm identifies valid signals are defined through

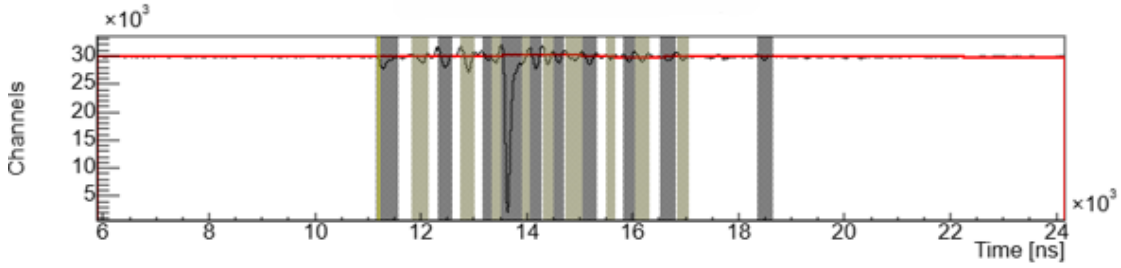

Figure 20: Raw signal registered by channel 7 of the LFMC - old version of the PSA routine.

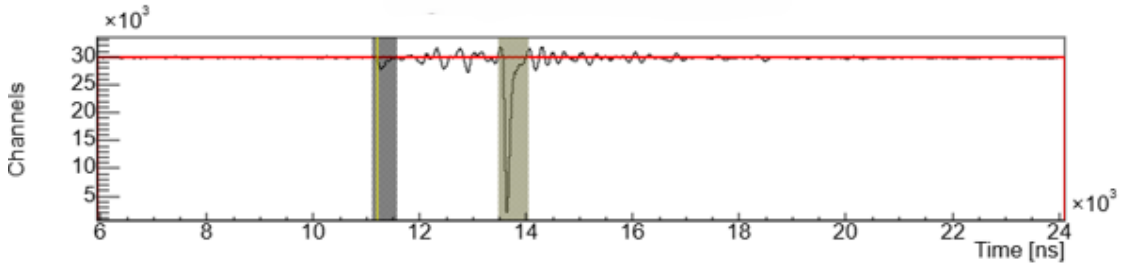

Figure 21: Raw signal registered by channel 7 of the LFMC - analysed with the new optimized version of the PSA.

constraints on some parameters, such as signal width, γ-flash time, pulse amplitude, and the ratio between the area and the amplitude of the signal. The parameters are defined and stored in a so-called *UserInput* configuration file, which is used for data decoding. There is a standard version of the UserInput file, that allows a preliminary reconstruction of signals, and which was used to process the signal shown in Figure 20. Since the PSA routine is a general purpose framework, the parameters used for the signal reconstruction are optimized for each detector and experimental campaign.

From Figure 20, it is possible to observe a region of pronounced oscillations following the γ-flash. These oscillations are induced by the intense burst of photons and relativistic particles produced in the spallation reaction, which temporarily perturbs the LMFC detector. Since these structures do not correspond to genuine neutron-induced events, they should not be reconstructed as valid signals. However, the PSA routine defined by the standard UserInput, incorrectly identifies this oscillatory region as containing event signals. This behaviour provides a clear example of the need for PSA optimization in order to improve data quality. By adjusting the selection ranges of several parameters, the signal reconstruction was improved. Figure 21 shows the same waveform presented in Figure 20, reconstructed using the optimized PSA routine. After the optimization, the PSA correctly selects only the γ-flash pulse and the large-amplitude

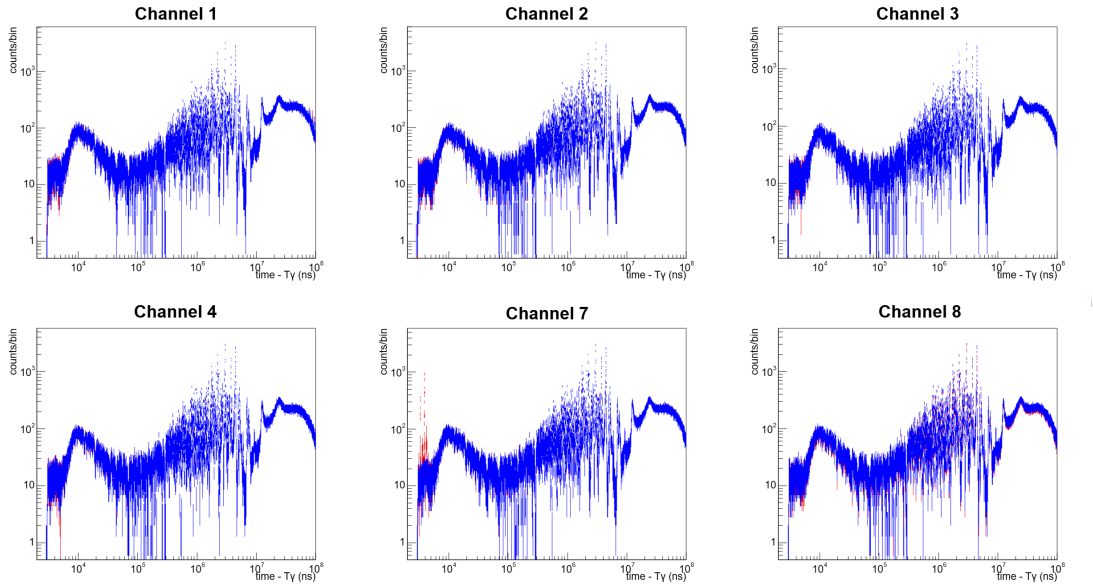

Figure 22: Time-of-flight histograms of Sample-in runs of the six active channels of the LFMC. Histograms obtained using data processed with the previous version of the User-Input file are shown in red, while those derived from data processed with the optimized version are shown in blue.

peak, which corresponds to a neutron-induced fission fragment event.

All experimental data were subsequently reprocessed using the optimized PSA routine, defined by the parameters stored in the new UserInput file.

The impact of the optimization was evaluated through a comparison of time-of-flight histograms built using data processed with the old and the new UserInput files. They are reported, for Sample-in data, in Figure 22, distinguishing each LMFC channel. The most significant changes in TOF histograms are observed for channels 7 and 8. These were indeed the channels most affected by γ-flash-induced oscillations, as was already evident from the inspection of their raw signals (such as Figure 20). Other channels were less affected from oscillations and the reconstruction of signals was therefore already efficient with the old version of the PSA. In these cases, PSA optimization has a smaller impact compared to channels 7 and 8, as can be seen from the comparison of their TOF histograms.

Figure 23 presents the TOF histograms for Sample-in runs of channel 7, along with their ratio. For this case, there is an evident reduction of noise at very low TOF. This indeed corresponds to the region just after the γ-flash, which is the one mostly affected by oscillations. Since low TOFs correspond to high energies, this work has improved the quality of the data at high neutron energies, which is the region of main interest for this experimental campaign.

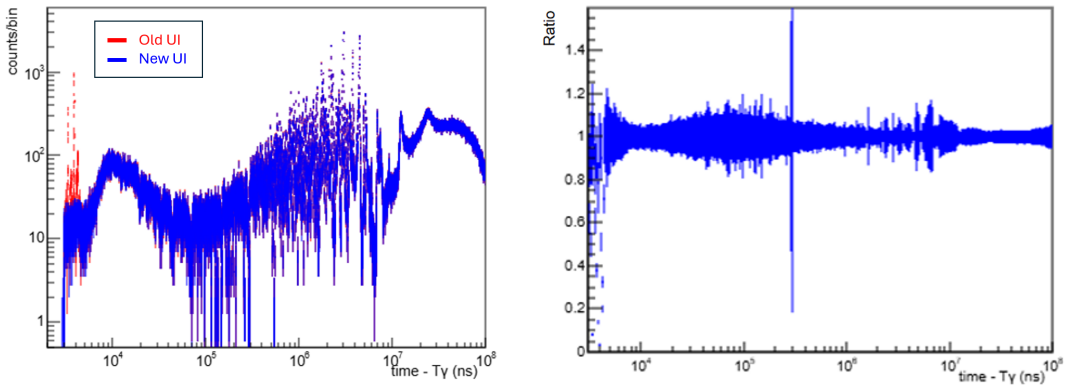

Figure 23: On the left: TOF histograms of Sample-in runs of channel 7, with data processed with the previous version of the UserInput file (in red) and the new one (in blue). On the right: ratio between the new UserInput and the old UserInput histograms. A significant reduction of oscillations at low TOF can be appreciated.

The reconstruction with new PSA routine has also significantly improved the statistics of channel 8, reaching 12% for the case of Sample-Out signals, as can be appreciated from Figure 24. For Sample-in data of the same channel, an increase of 5% was observed. This improvement, observed across the entire TOF range, is due to the fact that some signals were not properly reconstructed by the program before the optimization.

4.2 Amplitude Analysis

Once all data had been processed with the PSA algorithm optimized for this experiment, a detailed analysis of the amplitude spectra of the signals was carried out.

In Figure 25, a typical amplitude spectrum of data registered with the LMFC is presented. The spectrum exhibits two distinct peaks. The first one, located at lower amplitudes, is dominated by contributions from α particles emitted by the ^{235}U samples as a result of their natural radioactivity [40]. Since α particles deposit significantly less energy than fission fragments, they generate smaller-amplitude signals. The second structure, at higher amplitudes, corresponds to signals produced by fission fragments. Due to the limited energy resolution of the detector, light and heavy fission fragments cannot be resolved and therefore contribute to the same broad peak.

Since the α particles represent a source of background in this experiment, an amplitude selection cut was defined. Only signals with amplitudes above this threshold, corresponding to fission events, were retained and used for the construction of the Time-of-Flight and cross section histograms.

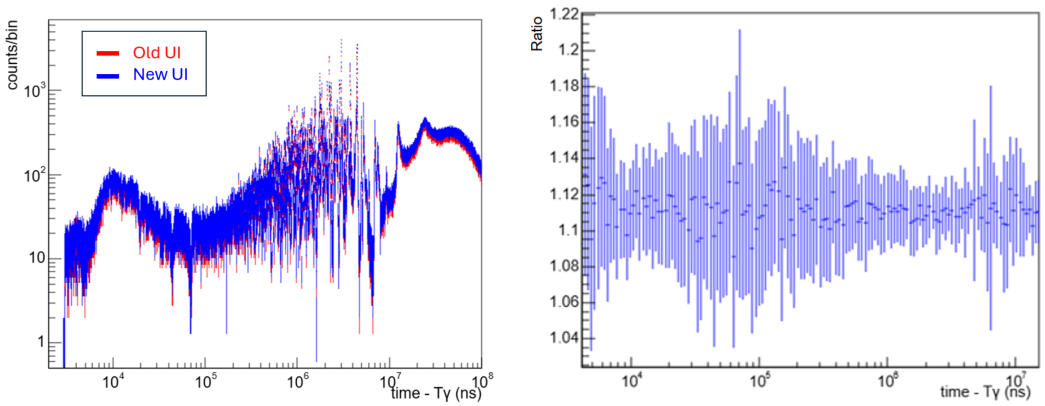

Figure 24: On the left: TOF histograms of Sample-out runs of channel 8, with data processed with the previous version of the of the UserInput file (in red) and the new one (in blue). On the right: ratio between the TOF histograms corresponding to the new and the old UserInput files. This comparison highlights an increase in statistics of approximately 12%.

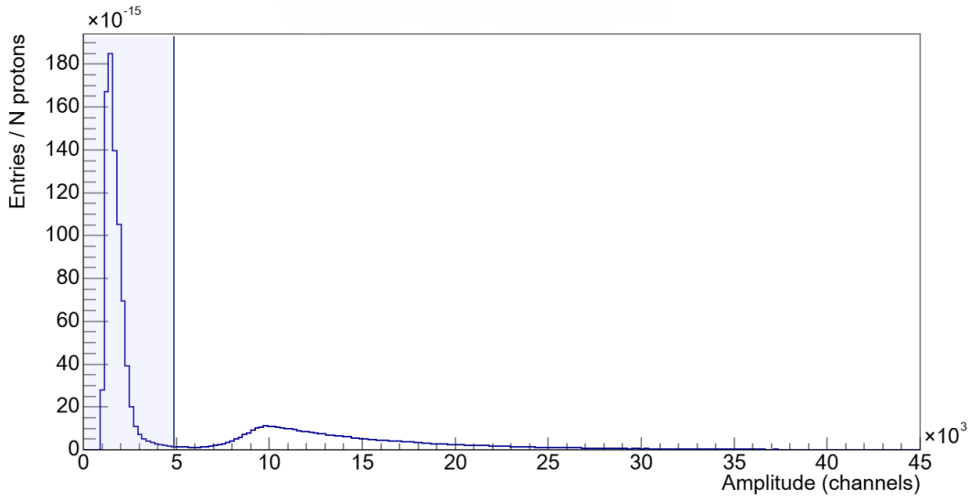

Figure 25: Typical amplitude spectrum obtained from LMFC data. The histogram was built with data acquired during the first week of measurements, in the Sample-in configuration, and for channel 3. The vertical line marks the amplitude threshold that distinguishes the background region (shadowed) from the fission events signals.

The analysis of the amplitude spectra is therefore fundamental for defining the selection criteria to distinguish neutron-induced signals from background. The amplitude spectra considered in the analysis were all normalized for the number of incident protons, so as to make more reliable comparisons.

A preliminary analysis of the amplitude spectra for each channel, which led to a first determination of the selection cuts, was carried out by grouping multiple runs together and is described in Section 4.2.1. Then, a quantitative evaluation of the detector stability was performed by monitoring the fission fragment peak position and detector efficiency over time (Section 4.2.2). A deeper analysis of the efficiency, which led to a data selection and to an estimate of the systematic uncertainty associated with the choice of the amplitude threshold, is described in Section 4.2.3.

4.2.1 Preliminary analysis of amplitude spectra

A first qualitative study of the amplitude spectra was performed in order to obtain a general overview of the detector behaviour over time. 14 groups of 3 consecutive runs, equally distributed throughout the experimental campaign, were selected and their corresponding amplitude spectra were compared and analysed. Figure 26 shows the amplitude spectra of these 14 groups for the case of channel 3.

From the figure, it is possible to observe that data acquired in the Sample-in configuration exhibit fewer events than those acquired in the Sample-out configuration, since in this case a fraction of the neutrons interact with the copper sample and therefore do not reach the detector. The most relevant feature of this plot is that the shape of the amplitude spectra remains stable over time, indicating that the detector response did not undergo significant variations during the measurement campaign. This stability allowed the use, for each channel, of a constant amplitude threshold for the whole campaign, without the need to introduce time-dependent selection criteria. The amplitude threshold was chosen in the valley region between the background and the fission peaks, as a compromise between rejecting as much background as possible and retaining all fission-fragment events. For example, the amplitude threshold for channel 3 was set to 5×10^3 channels. The six LMFC channels exhibit different shapes in their amplitude spectra, and therefore the choice of the amplitude threshold was performed separately for each channel. Table 4 summarizes the amplitude thresholds selected for the six channels, based on the analysis of their amplitude spectra.

LMFC channel	Amplitude threshold (channels)
Channel 1	4.5×10^3
Channel 2	5.5×10^3
Channel 3	5.0×10^3
Channel 4	4.0×10^3
Channel 7	5.5×10^3
Channel 8	6.0×10^3

Table 4: Initial choice of amplitude thresholds for the six channels of the LFMC.

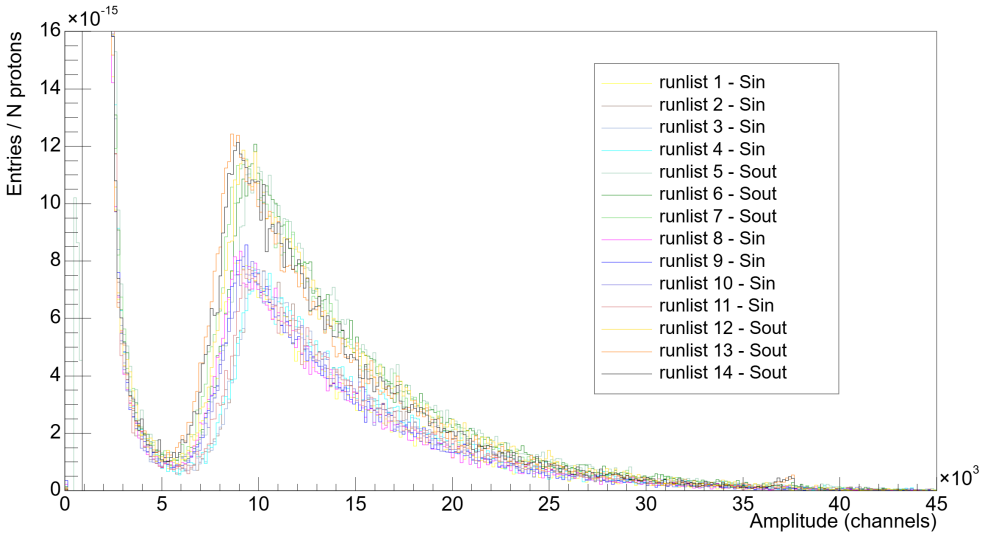

Figure 26: Amplitude spectra for channel 3 of the 14 groups of 3 consecutive runs, equally distributed throughout the campaign. The legend indicates, for each group, the configuration in which the data were acquired (Sin for Sample-in data and Sout for Sample-out). The vertical scale was truncated at 1.6×10^{-14} entries/protons, to better highlight the region between the two peaks.

4.2.2 Detector Stability Analysis

Once the amplitude thresholds were chosen, only the region above the threshold, corresponding to the fission-fragment peak, was considered. The amplitude spectra above threshold were computed separately for each run, as shown in Figure 27. From these histograms, two quantities were extracted:

- The detection efficiency, computed as the number of counts above threshold, normalized to the number of protons
- The amplitude corresponding to the position of the fission-fragment peak

The former quantity was computed as the integral under the curve shown in Figure 27 and provides a measure of the detector ability in detecting fission events. The latter was extracted by identifying the bin with the maximum number of entries and taking the central value of that bin. Both quantities were evaluated for each run and subsequently grouped into graphs as a function of the run number. The analysis was carried out separately for each of the six LMFC channels, and Sample-in and Sample-out data were treated independently. Runs corresponding to different weeks of measurement (already specified in Table 2) were displayed using different colours, in order to highlight possible time-dependent effects.

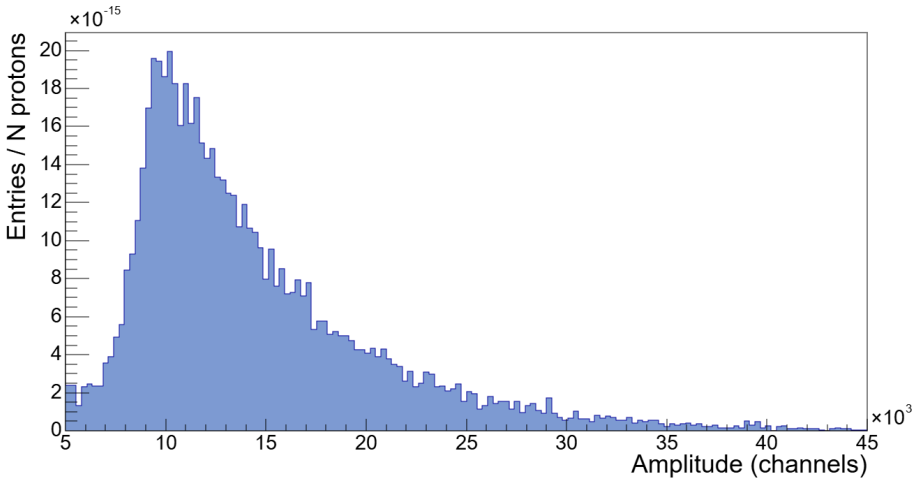

Figure 27: Amplitude spectrum above threshold for channel 3 of a Sample-out configuration run.

Figure 28 shows representative examples of these graphs for the Sample-out configuration of channel 3, displaying (a) the detection efficiency and (b) the position of the fission-fragment peak as a function of the run number. These graphs were produced to quantitatively assess the stability of the detector response over time for all six channels. From their analysis, some anomalous behaviours were identified. A small number of outliers were observed, and investigated in detail by inspecting their corresponding amplitude spectra and comparing them with those of adjacent runs. Figure 29 presents an example of such case. The outlier circled in Figure 29 (a) corresponds to a distorted shape of the amplitude spectrum, visible in Figure 29 (b), which might have been caused by a temporary instability of the detection system. Data that showed this behaviour were considered unreliable and were therefore disregarded from the analysis. Only a very limited number of runs exhibited this behaviour, and their exclusion did not result in any significant loss of statistics.

Outliers were not necessarily present simultaneously in both the efficiency and peak-position distributions. The combined analysis of the two types of graphs was therefore essential for the identification of all problematic runs.

Overall, small statistical fluctuations were observed, but no systematic trends were found, indicating that no significant gain shift occurred during the experimental campaign.

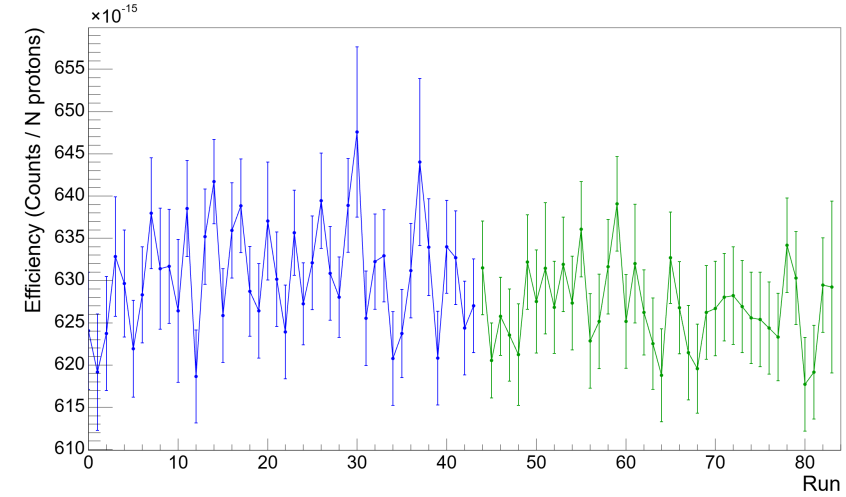

(a)

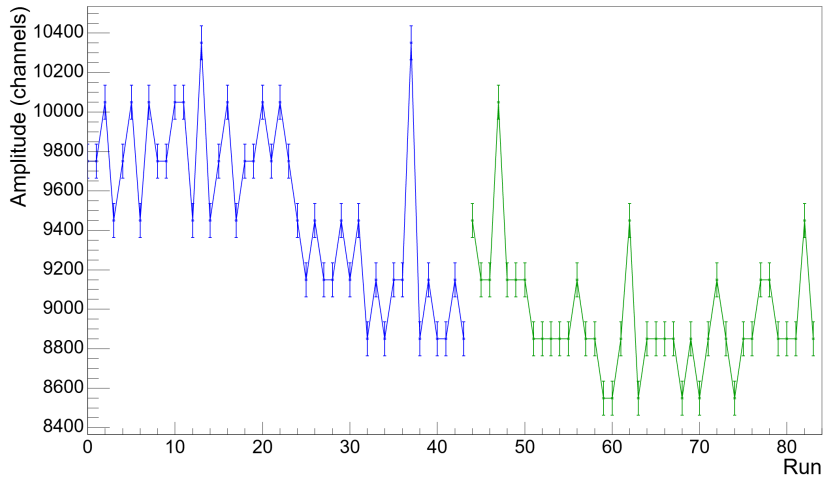

(b)

Figure 28: Detection efficiency (a) and position of fission fragment peak (b) as a function of the run number, for Sample-out runs of channel 3.

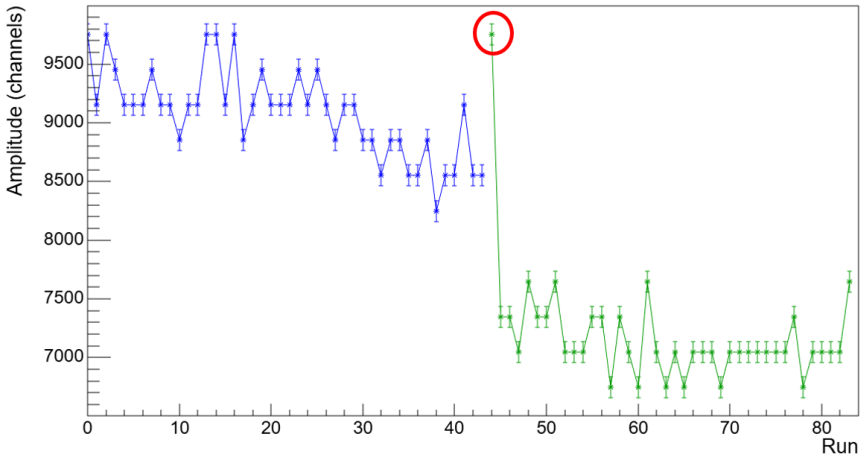

(a)

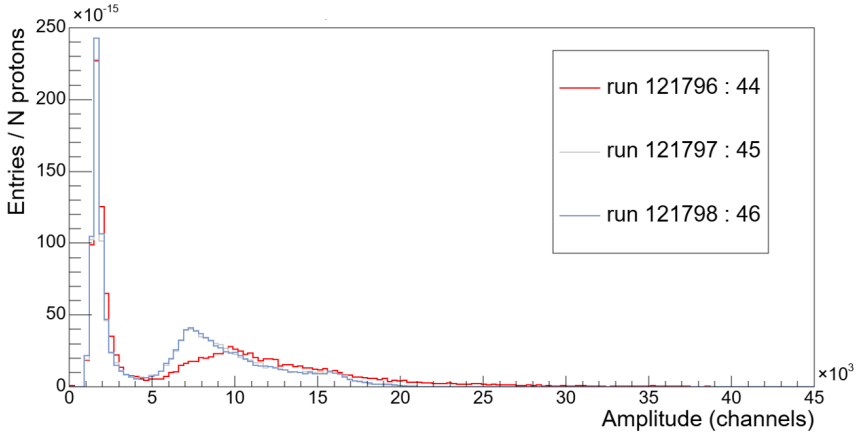

(b)

Figure 29: (a): Position of maximum amplitude for Sample-out runs of channel 1. Run number 44 constitutes an outlier and is circled in red. (b): Full amplitude spectra of runs 44 (in red), 45 and 46.

4.2.3 Efficiency analysis

For transmission experiments, it is particularly important to assess the stability of the detection efficiency over time, since this quantity plays a crucial role in assessing the reliability of the method. For this reason, a more detailed analysis of the efficiency was carried out. In the plots, data corresponding to different weeks of measurements were displayed using different colours, as visible in Figure 28 (a). The efficiency values belonging to each group were then collected into separate histograms, as illustrated in Figure 30. These histograms exhibited an approximately Gaussian shape and their

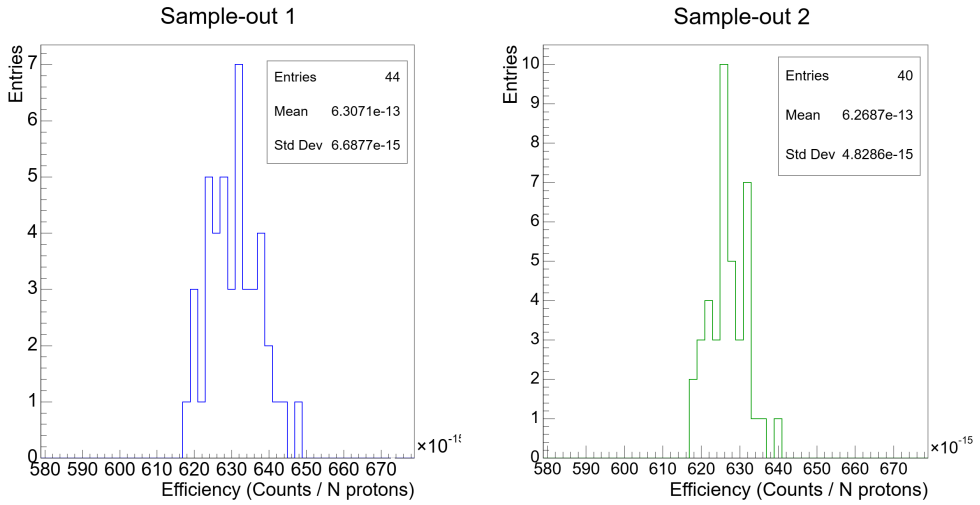

Figure 30: Histograms grouping the efficiency values of the 2 Sample-out weeks for channel 3 data. The legend displays the mean and standard deviation for each of these gaussian-shaped histograms.

mean μ and standard deviation σ values were extracted. Figure 31 shows the same efficiency graph as Figure 28 (a), with the addition of these reference lines.

For all channels and for both Sample-in and Sample-out configurations, the great majority of the efficiency values lie within $\pm 2\sigma$ from the mean value. For most cases, 2σ corresponds to approximately 2% of the efficiency value. This important result demonstrates that the detector efficiency remained sufficiently stable throughout the measurement campaign. This stability is a key requirement for the reliability of transmission measurements, as it ensures that possible variations in detector response do not introduce systematic effects in the determination of the cross section, thus validating the transmission method described in Section 3.1.

Data selection In order to improve the accuracy of the data, a data selection was performed by excluding the runs whose efficiency values lay more than 2σ from the

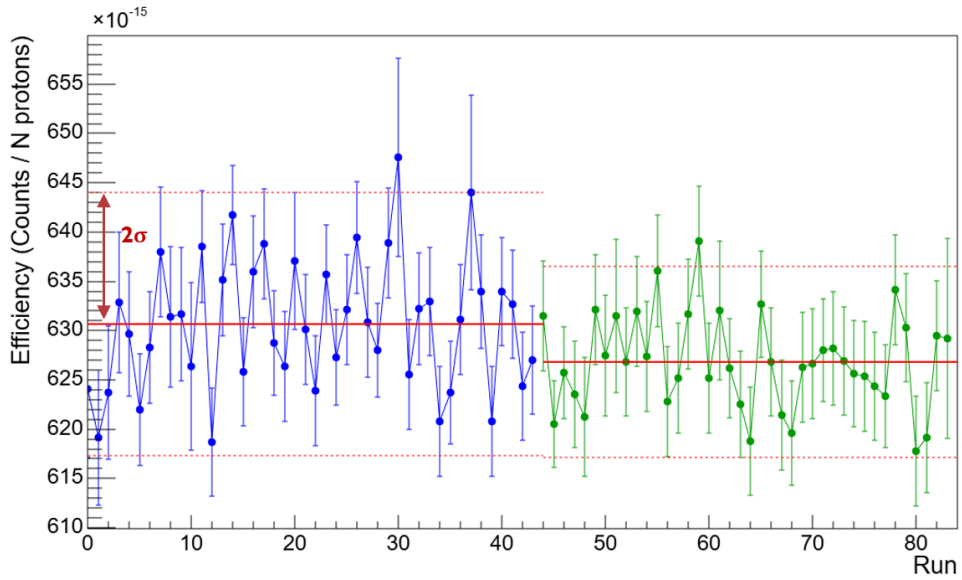

Figure 31: Detection efficiency as a function of the run number for Sample-out runs of channel 3. The continuous line is drawn in correspondence of the mean efficiency value, while the dashed lines are drawn at $\pm 2\sigma$ from the mean.

mean value, i.e. outside the region delimited by the two dashed lines in Figure 31.

The loss of statistics associated with this selection was evaluated and found to be, on average, approximately 4%, both in terms of reduced number of protons and events. Since this does not represent a significant loss, the selection was applied in favour of an enhanced data accuracy.

Efficiency dependence on amplitude threshold The impact of the choice of the amplitude threshold on the efficiency was also investigated. For each channel, two additional threshold values were considered, one lower and one higher than the value previously determined, reported in Table 4. For each of these alternative thresholds, efficiency graphs of the same type as those shown in Fig. 31 were reconstructed.

For each case, the mean efficiencies, along with the standard deviations, were extracted. Table 5 summarizes the results of this study for channel 3 of the LMFC.

For each configuration, the ratio between the mean and the standard deviation is also reported, expressed as a percentage. This value is of the order of 1%, indicating that the efficiency is considerably stable.

By comparing the different rows, it is possible to quantify the impact that a variation of the amplitude threshold has on the efficiency values. These results were used to estimate the systematic uncertainty associated with the choice of the amplitude threshold,

Threshold	Sample-in 1			Sample-in 2			Sample-out 1			Sample-out 2		
(channels)	μ	σ	σ/μ	μ	σ	σ/μ	μ	σ	σ/μ	μ	σ	σ/μ
4.5×10^3	4.27	0.05	1.19%	4.24	0.05	1.17%	6.36	0.07	1.07%	6.32	0.05	0.78%
5.0×10^3	4.23	0.05	1.20%	4.21	0.05	1.19%	6.31	0.07	1.06%	6.27	0.05	0.77%
5.5×10^3	4.20	0.05	1.23%	4.18	0.05	1.20%	6.27	0.07	1.07%	6.23	0.05	0.78%

Table 5: Results of the efficiency study for different amplitude thresholds on LMFC channel 3 data. The mean efficiency, μ, and the standard deviation, σ, are in units of 10^{-13} normalized counts.

defined as

$$\Delta\sigma_{amp\,thr} = \frac{\mu_{lower\,thr} - \mu_{upper\,thr}}{\mu_{central\,thr}} \tag{10}$$

The study was repeated for each LMFC channel, and it was verified that the resulting $\Delta\sigma_{amp\,thr}$ values always remained close to 1%. Consequently, a value of $\Delta\sigma_{amp\,thr} = 1\%$ was adopted as the systematic uncertainty associated with the choice of the amplitude threshold for the entire dataset. It is worth noting that, in most cases, the threshold values were varied by about 500 channels, which is a relatively large variation compared to the width of the region between the two peaks. This implies that the estimated uncertainty is likely an overestimation.

This contribution was subsequently combined with the other sources of uncertainty affecting the final cross section values, as will be discussed in Section 4.4.

4.2.4 α-induced background study

A possible presence of residual background in the selected events was investigated through a comparison of the amplitude spectra of dedicated and parasitic bunches.

The main contribution to the background events is represented by α particles released from ^{235}U decay, and is therefore constant over time. Considering that the time acquisition window is the same for parasitic and detected bunches, the number of background events from α particles are expected to be equal in the two cases. The number of fission events, instead, changes because the parasitic pulses present fewer neutrons per bunch with respect to dedicated ones. Once the normalization for the incident number of protons is performed, the fragment peaks overlap, while the peaks populated by the background events show different heights, as expected. This is indeed what is observed in Figure 32, which presents this comparison for channel 3. Figure 33 presents

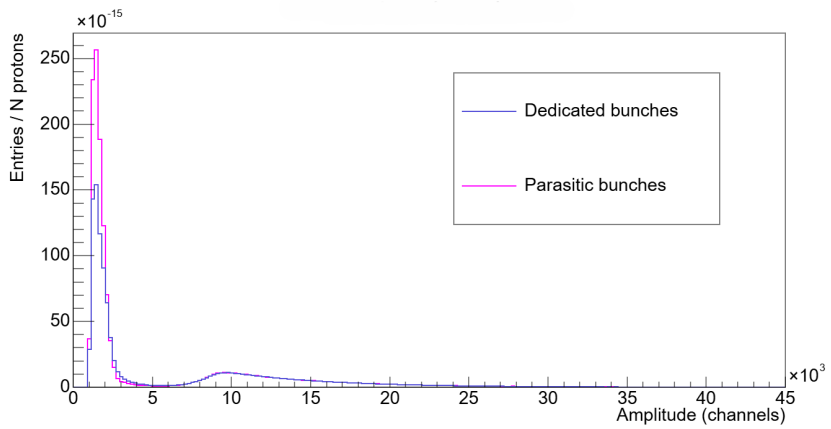

Figure 32: Amplitude spectra of dedicated and parasitic bunches for Sample-in data of channel 3.

the same spectra but only for amplitudes above the threshold that was chosen for that channel. In the same Figure, a ratio of the two histograms is shown.

The difference that is observed at amplitudes higher than the threshold suggests the presence of residual background. Since this behaviour was observed for all the channels, the six amplitude thresholds were all raised systematically by 500 channels, in order to exclude residual background events. The new thresholds, which are the ones that were used as selection cuts in the final analysis, are reported in Table 6.

This study constituted the last step of the amplitude analysis. The following Section describes the analysis of the Time-of-Flight and the construction of transmission histograms.

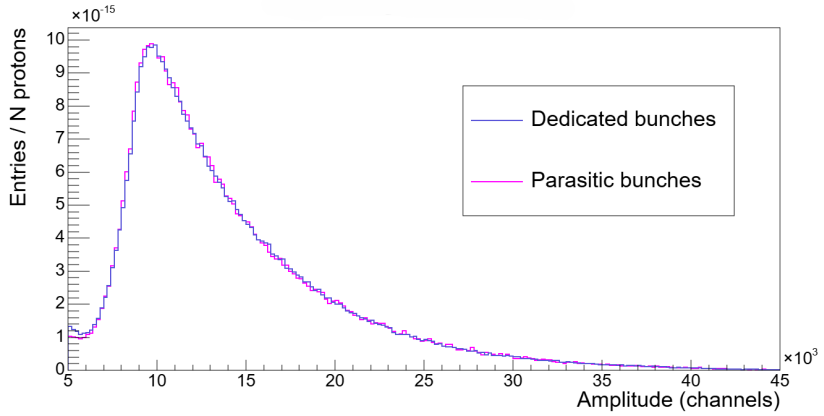

(a)

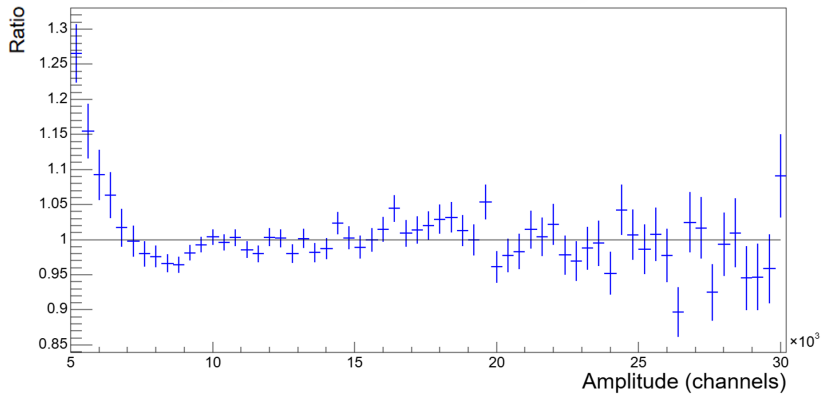

(b)

Figure 33: (a): Amplitude spectra above threshold of dedicated and parasitic bunches, for Sample-in data of channel 3; (b): ratio of the histograms corresponding to dedicated and parasitic bunches. The difference observed at amplitudes higher than the threshold suggests the presence of residual background.

Channel of LMFC	Amplitude threshold (channels)
Channel 1	5.0×10^3
Channel 2	6.0×10^3
Channel 3	5.5×10^3
Channel 4	4.5×10^3
Channel 7	6.0×10^3
Channel 8	6.5×10^3

Table 6: Final amplitude thresholds for the six channels of the LFMC.

4.3 Time-of-Flight analysis

This Section describes the analysis concerning the TOF spectra. In order to compute the exact TOF, the time registered by the detector needs to be corrected for the start time, as explained in section 2.3.1. This time was extracted from the PKUP detector, and then calibrated to match the γ-flash signals, as described in Section 4.3.1. Then, TOF histograms were computed for Sample-in and Sample-out data and, from their ratio, transmission histograms were extracted (Section 4.3.2). Section 4.3.3 describes the assessment of the compatibility of different datasets through both a qualitative and quantitative comparison of their TOF and transmission histograms. Finally, a calibration from TOF to neutron energy was performed by the extraction of the flight path, and is described in Section 4.3.4.

It is important to note that all the studies that follow were performed on data that was selected following the efficiency studies described in Section 4.2.3 and applying the amplitude selection cuts reported in Table 6 of Section 4.2.4.

4.3.1 γ-flash calibration

As already discussed in Section 2.3.1, in order to compute the proper TOF of incoming neutrons, the detection time of events registered with the LMFC must be corrected for a starting time that corresponds to the instant of neutron production. Usually at n_TOF, the γ-flash is used for this purpose. The γ-flash arrival time distribution was analysed and is shown, for Sample-in runs of channel 3, in Figure 34. This distribution, which is similar for the other channels, is relatively broad, with a width exceeding 200 ns. The time distribution of signals detected by the PKUP detector was also examined (Figure 35) and resulted to be much narrower, with most signals concentrated in only 40 ns. This indicates that the PKUP detector provides a much more precise time information with respect to the γ-flash recorded with the LMFC. For this reason, the time signals registered by the PKUP were employed in the analysis as the start-time reference.

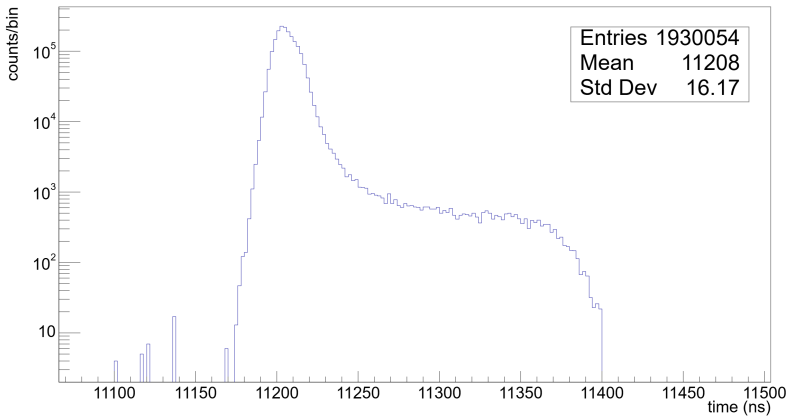

Figure 34: Distribution of the γ-flash times registered by channel 3 of the LMFC for Sample-in runs.

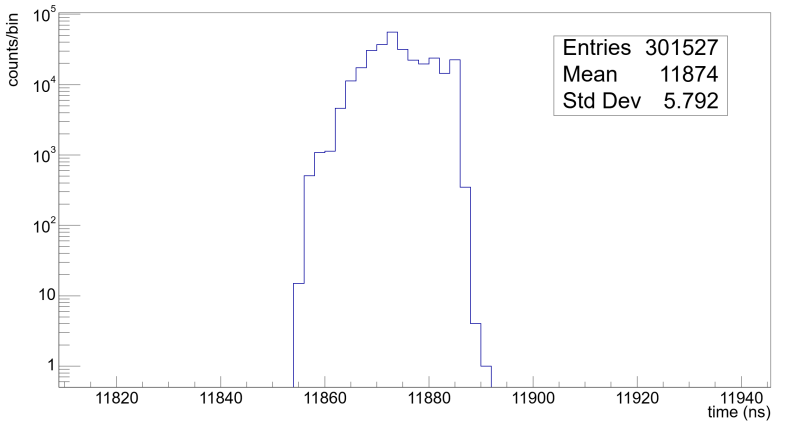

Figure 35: Time distribution of the PKUP detector signals for Sample-in runs.

In order to match the correct timing information, which is the instant of neutron production, the PKUP signal had to be calibrated. The calibration was performed by simply computing the difference between the the γ-flash time and the time registered by the PKUP for each proton bunch. These values were grouped into a histogram, on which a Gaussian fit was performed to extract the mean value. This calibration procedure was performed independently for the six active LMFC channels, and the results are reported in Figure 36.

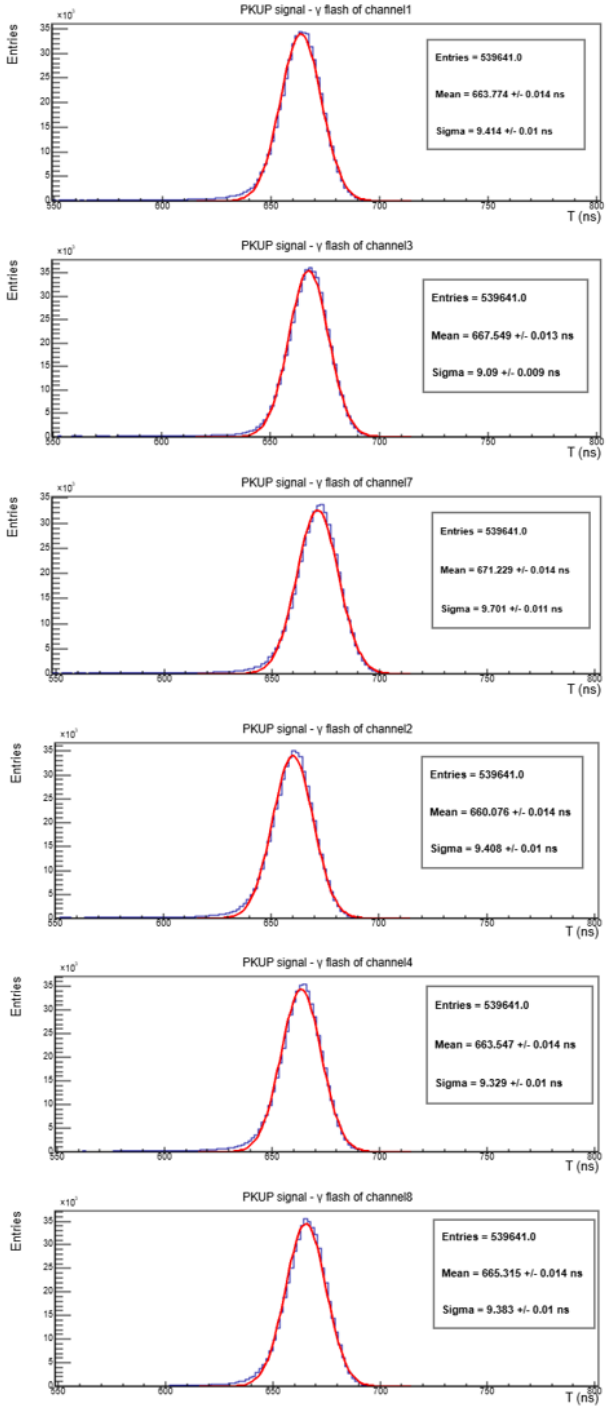

Figure 36: Calibration of the PKUP time signals to match the γ-flash registered by the six channels of the LMFC.

The mean values are approximately 660 ns, but they differ by several nanoseconds among the various channels. For this reason, six different calibration values (referred to as Δ) were extracted and applied independently in the construction of the TOF histograms.

4.3.2 TOF and transmission histograms

Time-of-flight histograms were finally constructed on data selected following the efficiency study described in section 4.2.3, applying the amplitude cuts reported in Table 6 and the timing calibration described in section 4.3.1. Furthermore, a selection condition was also applied on time, by selecting events that satisfy the condition TOF-$T_{PKUP} \geq 10^3$ ns. This cut is motivated by the fact that the region immediately following the γ-flash is characterized by a great instability, since the tail of the γ-flash signal may not have completely vanished yet. In this region, effects such as detector saturation can interfere with the data acquisition, making the data unreliable for the analysis. The imposed selection condition therefore ensures that that only events occurring in a time window where these transient effects are no longer present are retained. Finally, the selection condition on TOF introduces an upper limit on the maximum neutron energy of the cross section data. Details on the TOF to energy conversion are given in Section 4.3.4.

TOF histograms were built separately for Sample-in and Sample-out data, and they are displayed in Figure 37 for channel 3 of the LMFC.

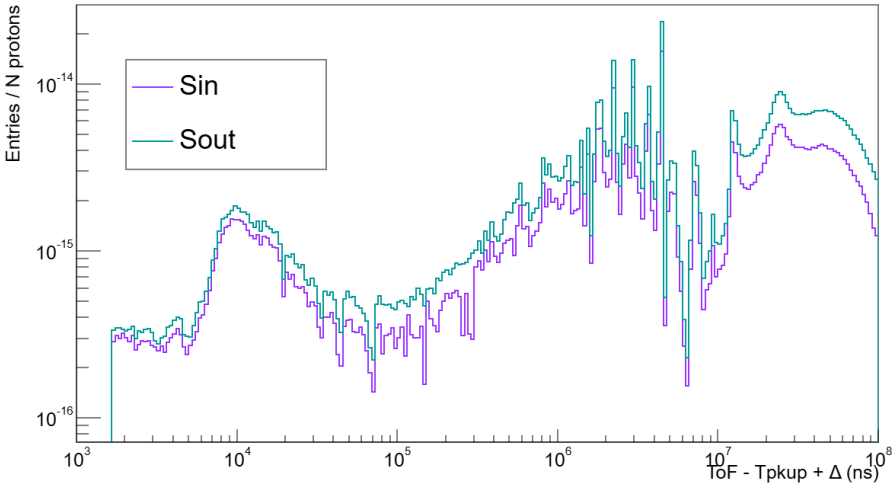

Figure 37: Calibrated Time-of-flight histograms of LMFC channel 3 data, for Sample-in (Sin) and Sample-out (Sout) runs.

It is worth recalling that Sample-in data correspond to data acquired with the copper sample in the beam, while Sample-out data were acquired without it, therefore any difference in the two histograms can be attributed to the presence of copper. The Sample-in histogram presents less counts with respect to Sample-out, since the copper sample absorbs a fraction of neutrons. This difference in the number of registered events is more evident in the high TOF region, which corresponds to low neutron en-

ergies. This is explained by the fact that, at low energies, the fraction of neutrons absorbed is higher, due to the typical behaviour of total neutron-induced cross sections as a function of energy.

From Figure 37, several structures can be observed. Some are present in both Sample-in and Sample-out histograms and can be attributed to neutron interactions with the structural materials of the LMFC, such as aluminium, but mainly uranium. The interactions of neutrons with the ^{235}U samples are likely the cause of the resonances observed in the region between 10^6 and 10^7 ns. The structures that are observed only in Sample-in data can be instead associated with neutron interactions with the copper sample.

From the ratio of Sample-in and Sample-out histograms, the transmission as a function of TOF can be extracted, as explained in Section 3.1. Figure 38 presents the transmission histogram for channel 3, obtained from the ratio of the two histograms of Figure 37.

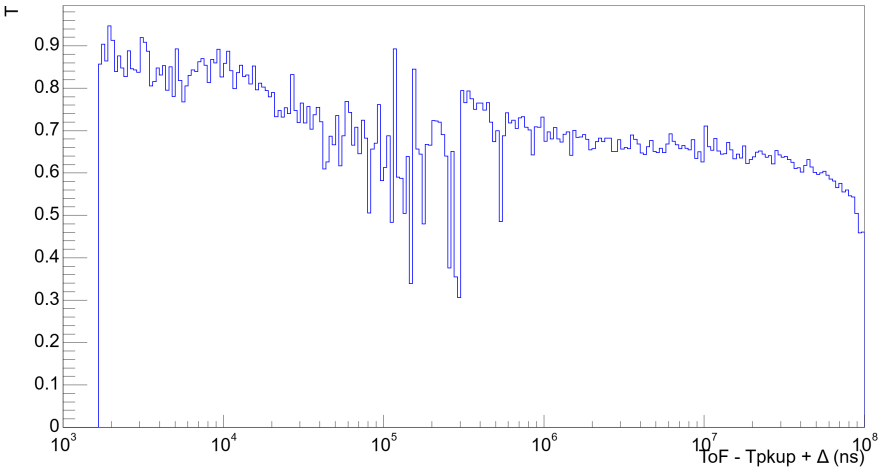

Figure 38: Transmission as a function of TOF for LMFC channel 3 data.

As expected, transmission values are always between 0 and 1. In principle, if no systematic effects are present between the Sample-in and Sample-out runs, the structures observed in both cases should cancel out when computing the transmission ratio. Indeed, the region between 10^6 and 10^7 ns, which shows many resonances in the TOF histograms, is almost flat in the transmission histogram. The structures that are still observed in the transmission histogram can instead be attributed to the interaction of neutrons with the copper sample.

These histograms were built separately for different datasets, and they were compared to assess the compatibility of the corresponding datasets, as described in Section 4.3.3.

4.3.3 Data compatibility assessment

The TOF and transmission histograms were built separately for different datasets and then compared in order to assess the compatibility of the corresponding data. Distinctions were made between data corresponding to different weeks of measurements, data registered by the different channels of the LMFC, and between data corresponding to dedicated and parasitic proton pulses.

Compatibility of data measured over different weeks Selecting data registered by only one LMFC channel, TOF histograms of Sample-in runs were built separately for data registered in the two different weeks of measurement corresponding to this configuration. This study was repeated separately for each channel of the LMFC and is presented in Figure 39 for channel 1 as a representative example.

Figure 39 (a) presents the two TOF histograms, with Sin 1 corresponding to the first week of the measurement campaign and Sin 2 to the third one (see Table 2 for the timeline). In order to make a quantitative comparison, the ratio of these two histograms was computed (Figure 39 (b)). From their ratio as a function of TOF, it is possible to observe small oscillations around 1, mostly within 5%. This behaviour is confirmed by the histogram presented in Figure 39 (c), which groups the ratio values into a histogram, of which the mean value and standard deviation are extracted by means of a Gaussian fit. The mean ratio is compatible with 1 within a standard deviation of 3.6%. This indicates that the two histograms, and therefore also the corresponding datasets, are compatible. This represents a further confirmation of the stability of the detector over time, since no systematic differences were observed between data measured in different weeks.

This comparison was then repeated for Sample-out data, and is presented in Figure 40. The same conclusions can be drawn for this case, again with a compatibility of 1 within 4%.

Then, transmission histograms were computed separately for the first two weeks of measurement (Sin1/Sout1) and for the last two (Sin2/Sout2). Assessing the compatibility of the transmission histograms is important because the transmission is the quantity from which the cross section is directly extracted, as explained in Section 3.1.

The comparison is presented in Figure 41, again only for channel 1 data. Also in this case, some oscillations were observed in the ratios, but their values are compatible with 1 within 5.4%, indicating the absence of systematic effects. This is another confirmation of the stability of the detector over time, which allows the combination of the data acquired in the different time windows, without the need to apply time-dependent corrections.

As already mentioned, the results were presented here for LMFC channel 1 as an example, but similar values were found for the other channels of the LMFC, with compatibilities always within 5%.

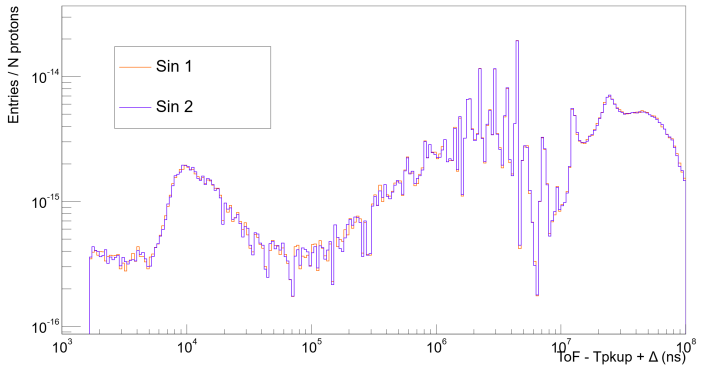

(a)

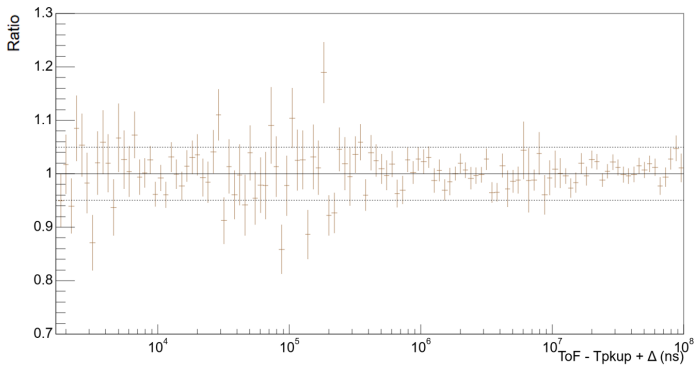

(b)

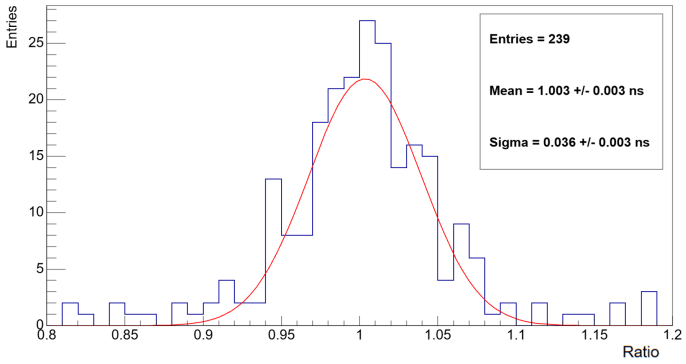

(C)

Figure 39: (a): TOF histograms of the two weeks of Sample-in (Sin 1: first week of measurement, Sin 2: third week), for LMFC channel 1 data; (b): ratio of the two histograms (Sin1/Sin2), with a continuous line traced at 1 and two dashed lines at $\pm$ 5% from 1; (c): ratio values distribution, fitted with a Gaussian function.

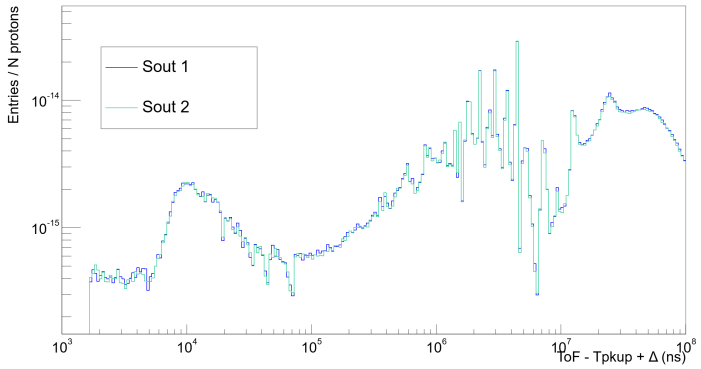

(a)

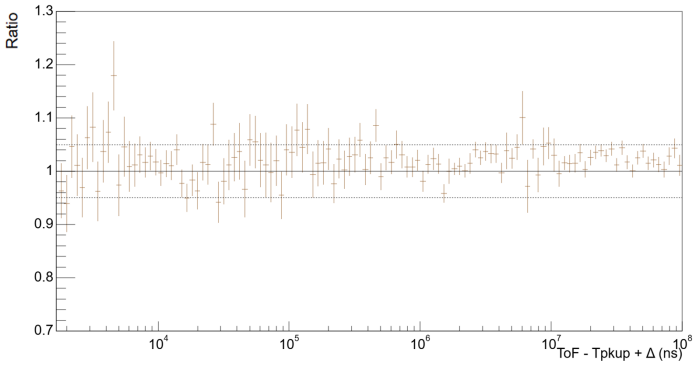

(b)

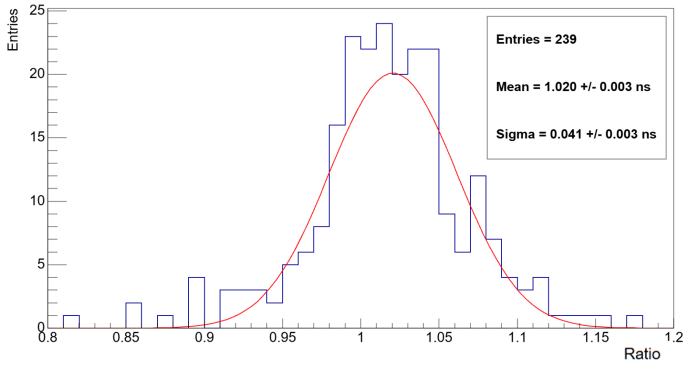

(C)

Figure 40: (a): TOF histograms of the two weeks of Sample-out (Sout 1: second week of measurement, Sout 2: fourth week), for LMFC channel 1 data; (b): corresponding ratio (Sout1/Sout2), with a continuous line traced at 1 and two dashed lines at $\pm$ 5% from 1; (c): ratio values distribution, fitted with a Gaussian function.

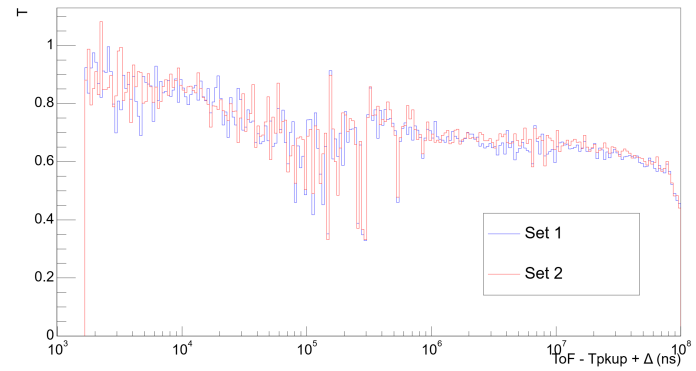

(a)

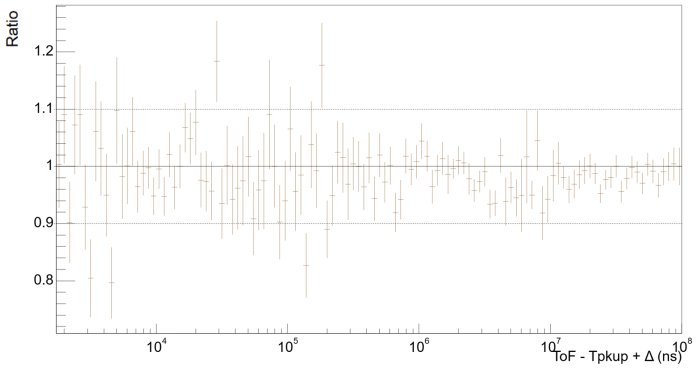

(b)

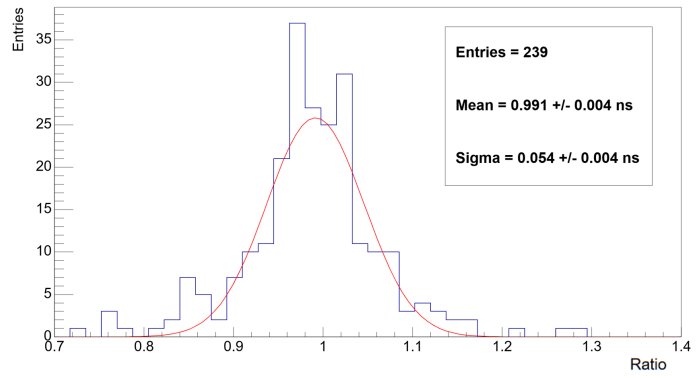

(c)

Figure 41: (a): Transmission histograms of the first two weeks of measurement (Set 1) and the last two week of measurement (Set2), for LMFC channel 1 data; (b): corresponding ratio (Set1/Set2), with a continuous line traced at 1 and two dashed lines at $\pm$ 10% from 1; (c): ratio values distribution, fitted with a Gaussian function.

Compatibility of the LMFC channels The compatibility of the six channels of the LMFC was then assessed through a comparison of their transmission histograms. The channels were compared in pairs, and Figure 42 presents the comparison of channel 1 with channel 4 as an example.

From Figure 42 (b), it is possible to observe that the values are compatible with 1 within 10% across the whole TOF range. Figure 42 (c) allows a more quantitative comparison, by grouping the ratios into a histogram fitted with a Gaussian function. From the results of the fit, it is possible to assess a compatibility with 1 within 4%.

Similar results were found for the other pairs, with no systematics observed, so it was concluded that the 6 channels are all compatible. This assessment allows the combination of data corresponding to different acquisition channels without having to correct for offsets.

Compatibility of dedicated and parasitic bunches The last compatibility check that was performed concerns the comparison between data corresponding to neutrons produced by parasitic and dedicated proton bunches impinging on the lead target. As explained in Section 2.1, these bunches have different intensities, so it was necessary to verify that no significant differences were present in the induced events. Their comparison was therefore carried out to ensure the compatibility of the two datasets and to justify their summation in the final analysis.

Figure 43 presents this comparison for LMFC channel 1 data.

Despite the oscillations and some outliers lying at specific TOFs, the data are compatible with 1 within 5.4%, without systematic effects. This confirms the possibility of combining the corresponding datasets.

Since all the compared datasets were judged compatible, they were combined together for the extraction of the final transmission spectrum.

Data corresponding to the two sets of Sample-in and Sample-out were summed together, and transmission histograms were computed distinguishing each channel and bunch type, obtaining thus 12 histograms. These were then summed into a single transmission histogram as a function of TOF. This was done because possible small systematic differences among the individual cases can partially cancel out when computing the ratio between Sample-in and Sample-out data, improving the overall reliability of the transmission measurement.

The resulting transmission histogram as a function of TOF is shown in Figure 44.

In order to convert this histogram from time to energy domain, a calibration procedure was carried out and is described in Section 4.3.4.

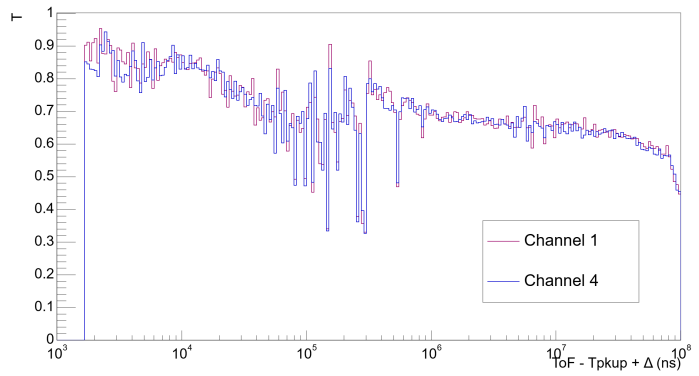

(a)

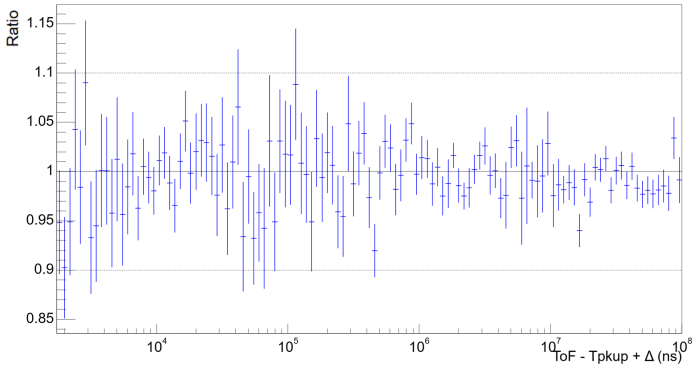

(b)

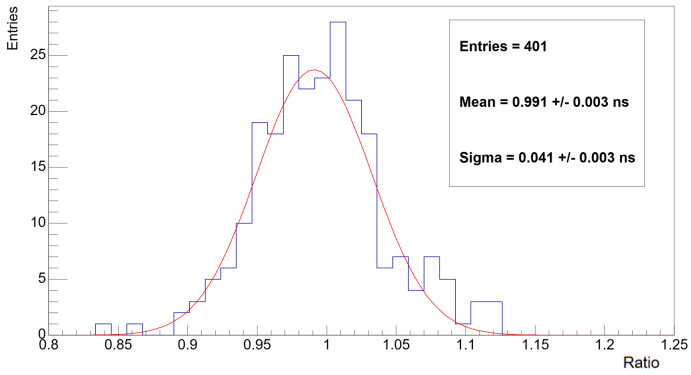

(c)

Figure 42: (a): Transmission histograms of LMFC channel 1 and 4; (b): corresponding ratio (channel 4 / channel 1), with a continuous line traced at 1 and two dashed lines at $\pm$ 10% from 1; (c): ratio values distribution, fitted with a Gaussian function.

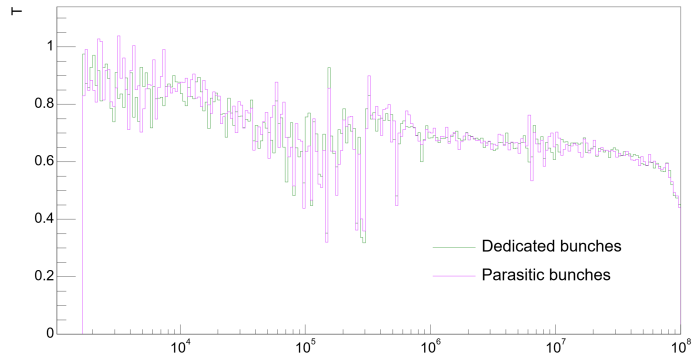

(a)

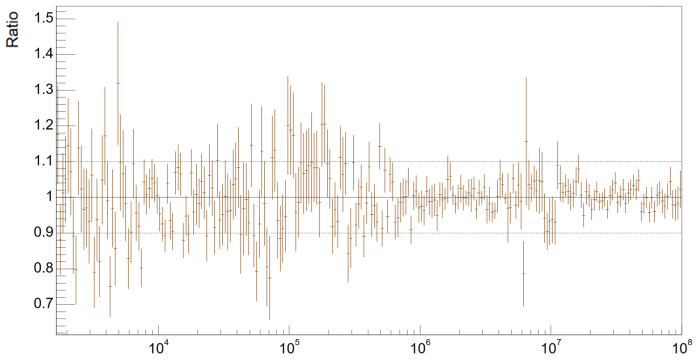

(b)

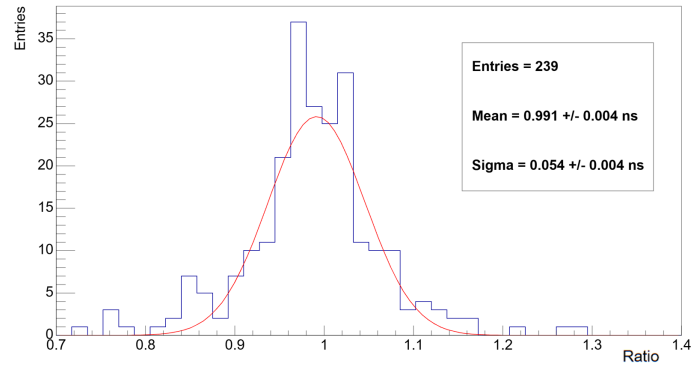

(c)

Figure 43: (a): Transmission histograms of data corresponding to dedicated and parasitic proton bunches, for LMFC channel 1; (b): corresponding ratio (dedicated / parasitic), with a continuous line traced at 1 and two dashed lines at $\pm$ 10% from 1; (c): ratio values distribution, fitted with a Gaussian function.

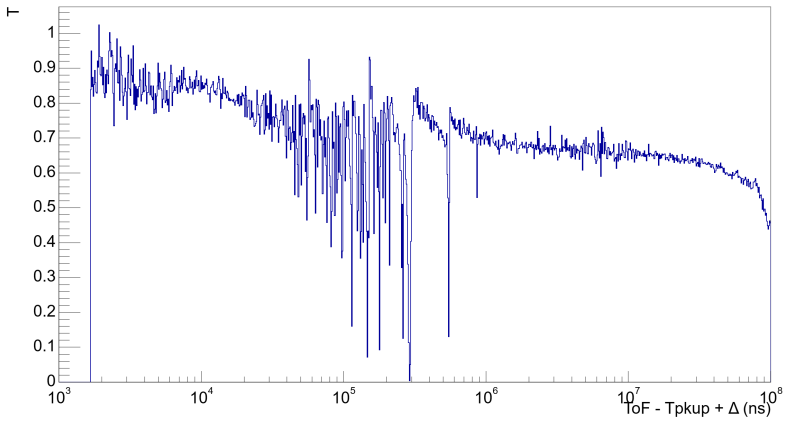

Figure 44: Final transmission histogram as a function of TOF. This histogram includes the whole data of the ^{nat}Cu transmission experimental campaign.

4.3.4 Time-of-Flight to energy calibration

A calibration procedure was carried out in order to convert the Time-of-Flight into neutron energy. The equation for this calibration can be obtained by combining the formulas in Eq.1 and Eq. 3 described in Section 2.2. In the low-energy regime, the classical expression (4) is valid, which, when combined with 1, leads to:

$$E_n = \frac{1}{2} m (\frac{L}{TOF})^2 \tag{11}$$

In order to perform the conversion from TOF to E_n, it is therefore necessary to know the exact neutron flight path (L). This value was extracted by matching several low-energy copper resonances observed in evaluated nuclear data with the corresponding resonances in the transmission spectrum. The energies of the resonances were taken from ENDF/B-VII.1 [42] (n,total) cross section data of the copper isotopes ^{63}Cu and ^{65}Cu, and are reported in Table 7, along with the indication of the isotope to which they correspond. The same resonances were identified in the transmission histogram of Figure 44. A Gaussian fit was performed on each resonance to extract the mean TOF, as shown in Figure 45. The mean TOF values obtained from the fits, together with their associated uncertainties, are reported in Table 7.

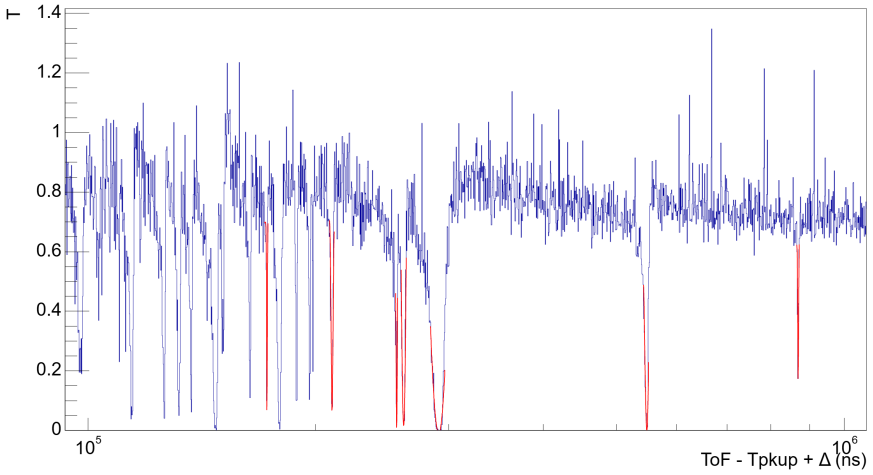

Figure 45: Gaussian fits applied to seven copper resonances in the transmission histogram. The fits allow the extraction of the mean TOF associated with each resonance.

Resonance	1° (^{65}Cu)	2° (^{63}Cu)	3° (^{63}Cu)	4° (^{65}Cu)	5°(^{63}Cu)	6° (^{65}Cu)	7° (^{63}Cu)
E_n (eV)	230	579	2038	2529	2642	3920	5831
TOF (ns)	868882 $\pm$ 92	548075 $\pm$ 49	290856 $\pm$ 65	261387 $\pm$ 32	255874 $\pm$ 24	210169 $\pm$ 30	172379 $\pm$ 31

Table 7: Seven low-energy copper resonances selected for the determination the flight path. The first row indicates the copper isotope for which each resonance is observed. The second row presents their energies, taken from ENDF/B-VII.1 library [42], and the last row reports the corresponding TOF values obtained from Gaussian fits to the transmission histogram built with the LMFC data.

The values reported in Table 7 were then used to build an energy-TOF graph, shown in Figure 46. Each point of the plot corresponds to a copper (n,tot) resonance. A fit to these data was performed using the non-relativistic formula 11, since all selected resonances lie in the low-energy region. The flight path L was left as the only free parameter of the fit. The value of the flight path resulting from the fit is: L = 182.1 $\pm$ 0.1 m.

This value of L was then used to convert the entire transmission histogram from TOF to energy domain. Figure 47 shows the same histogram as Figure 44 but expressed as a function of neutron energy.

Finally, from this distribution, the total cross section histogram as a function of neutron energy can be extracted. The following section (4.4) describes the cross section histogram, which represents the main result of this thesis and the objective of the n+^{nat}Cu experiment.

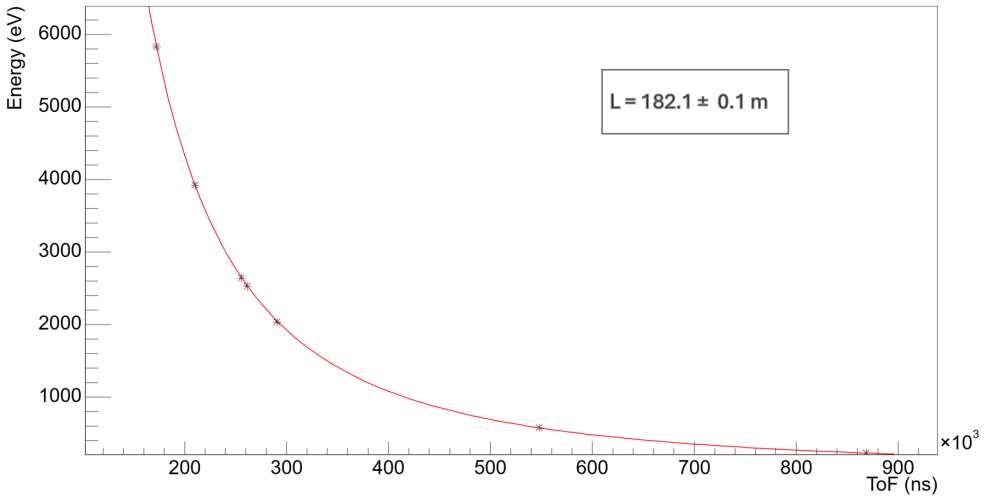

Figure 46: Neutron energy versus Time-of-Flight for several resonances of ^{63,65}Cu total cross sections. The energies were taken from ENDF/B-VII.1 library, while the TOF values were extracted from Gaussian fits to the corresponding resonances in the transmission histogram. The data were fitted with equation 11 to determine the neutron flight path.

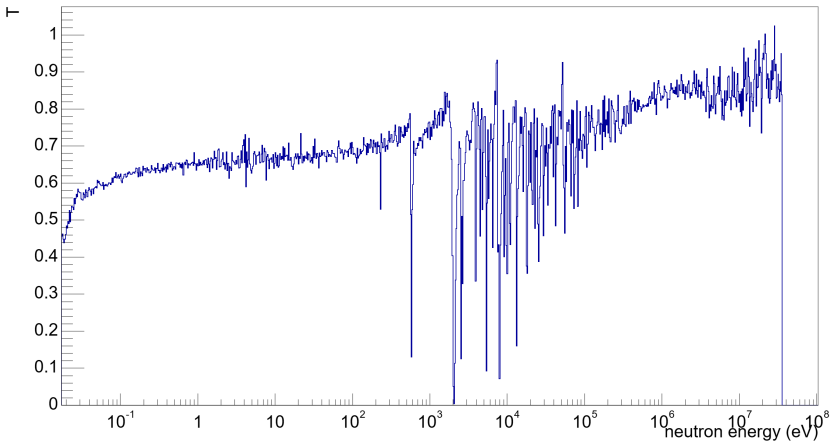

Figure 47: Final transmission histogram as a function of incident neutron kinetic energy.

4.4 Cross section

The histogram of the transmission as a function of neutron energy, shown in Figure 47, can be converted into cross section, as explained in Section 3.1. By knowing the areal density of the sample, this conversion can be made using equation 9. The areal density of natural copper was computed from the measured values of the sample mass and diameter and was found to be $n = (5.17 \pm 0.02) \times 10^{-2}$ atoms/barn.

Figure 48 shoes the ^{nat}Cu(n,tot) cross section as a function of neutron energy. The

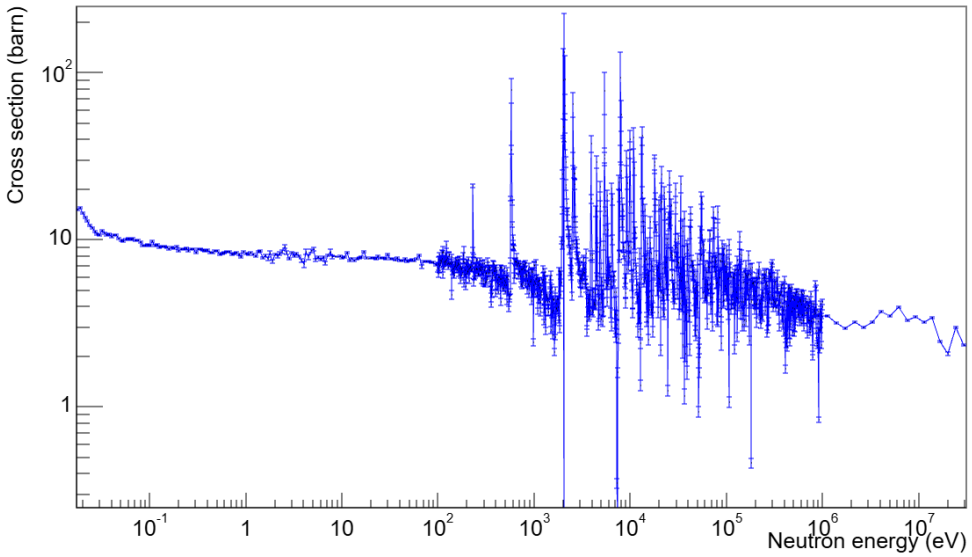

Figure 48: ^{nat}Cu(n,tot) cross section built with n_TOF data.

neutron energy covered spans from 10^{-2} eV to 30 MeV. The wide energy range covered demonstrates the quality of the data. In particular, providing data up to 30 MeV represents an important result, since extending copper cross sections to high neutron energies, i.e. to the MeV region, was the main motivation behind the experiment (see Section 1.5)

Three different binnings were used in this histogram, to best highlight the behaviour of a typical total cross section across different energy regions. Up to 10^2 eV, a binning of 80 bins per decade was employed. From 10^2 to 10^6 eV, the binning was increased to 500 bins per decade, to resolve the single resonances. Then, from 1 to 30 MeV, where the resonance spacing becomes too small to be resolved, a binning of 20 bins per decade was used. The high-energy region is characterized by strong oscillations, since the detector is affected by the γ-flash induced effects. These oscillations represent the main limitation for extending the analysis to even higher neutron energies and justify

the choice of a relatively low binning in this region.

The tailored choice of the binning allows to appreciate the different aspects that characterize each energy range. The low-energy region, extending from thermal neutrons up to a few tens of eV, is characterized by the typical 1/v behaviour. The flat trend observed in the logarithmic plot of Figure 48 is a direct manifestation of this dependence. A small deviation from this flat tendency can be observed at very low energies. This might be due to a slight misalignment or imprecise positioning of the copper sample, which could cause some non-negligible effects for very low energy neutrons, for which the interaction probability is particularly high.

The intermediate energy region exhibits many resonances, which are well resolved. Above approximately 1 MeV, the inelastic channel opens and a characteristic "bump" becomes visible in the cross section. As already mentioned, this region is affected by large oscillations, which limit the achievable precision of the data and imply an upper limit on the neutron energy.

Uncertainty evaluation There are several sources of uncertainty that contribute to the total error associated with the cross section. The error bars shown in the total cross section histogram of Figure 48 were computed as the statistical uncertainty associated with the number of counts in each bin (N), i.e. as the inverse of the square root of the number of counts

$$\Delta\sigma_{counts} = \frac{1}{\sqrt{N}}$$

This contribution depends on the chosen binning, since the number of events per bin varies with the bin width. There is also an uncertainty associated with the number of protons delivered to the target. However, this contribution is sufficiently small to be considered negligible. Another small contribution arises from the uncertainty on the areal density of the sample, which enters directly into the computation of the cross section. This uncertainty is given by:

$$\Delta\sigma_n = \frac{n}{\Delta n} = 0.4\%$$

Finally, there is the systematic uncertainty associated with the choice of the amplitude threshold, which was estimated with the efficiency study described in Section 4.2.3. It was verified that this value, for most detectors and also for Sample-in and Sample-out data, was stable around

$$\Delta\sigma_{amp\,thr} = 1\%$$

Since these contributions are independent, they were combined together through a quadrature sum, as follows:

$$\Delta\sigma_{tot} = \sqrt{(\Delta\sigma_{counts})^2 + (\Delta\sigma_n)^2 + (\Delta\sigma_{amp\,thr})^2} \tag{12}$$

Comparison with other experimental and evaluated data n_TOF cross section data were compared with other data, obtained from both independent experimental measurements and evaluated nuclear libraries, by overlapping the corresponding plots. From these comparisons, a systematic energy shift with respect to n_TOF data was observed.

The n_TOF data had been calibrated from TOF to energy using a flight path value of L = 182.1 m, which was determined through the resonance calibration method described in Section 4.3.4. This value might not exactly correspond to the true flight path and is therefore considered responsible for the systematic energy shift that is observed. This does not constitute a critical issue, since the (n,tot) data will eventually be combined with capture cross sections measured at n_TOF as part of the RAMEN initiative. In that context, the flight path will be re-evaluated more accurately, and the value determined here should therefore be considered preliminary rather than final. For this reason, conversions using different values of the flight path were tested and the comparison with the other datasets was repeated. The flight path value that provided the best agreement with the external data was found to be L = 182.5 m.

All cross section histograms presented in this thesis (including Figure 48) have therefore been constructed using this value for the TOF-to-energy conversion.

In Figure 49, a comparison of n_TOF cross section data with experimental data of the ORELA facility [21] is presented.

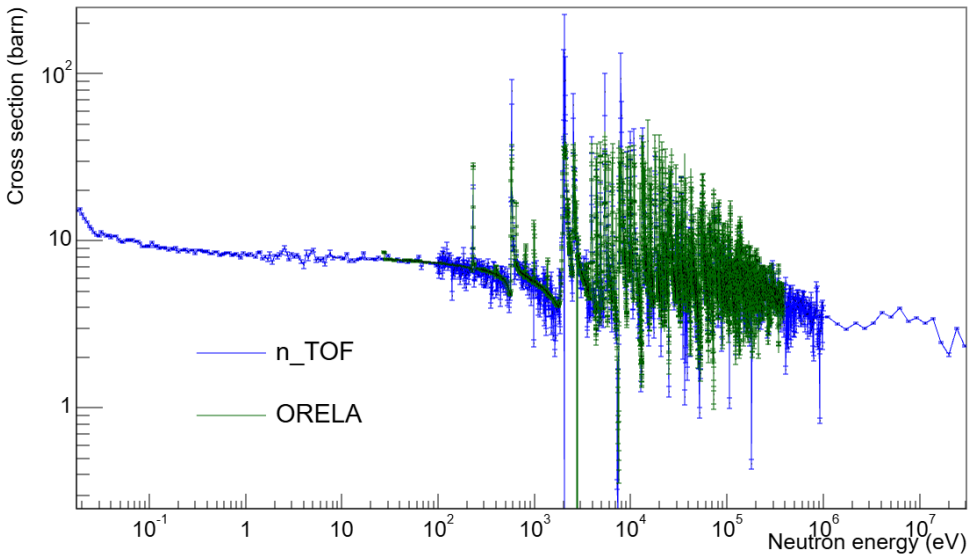

Figure 49: ^{nat}Cu(n,tot) cross section of n_TOF (in blue) and ORELA data (in green).

It is evident that n_TOF data extend the energy range of cross section data. In Figure

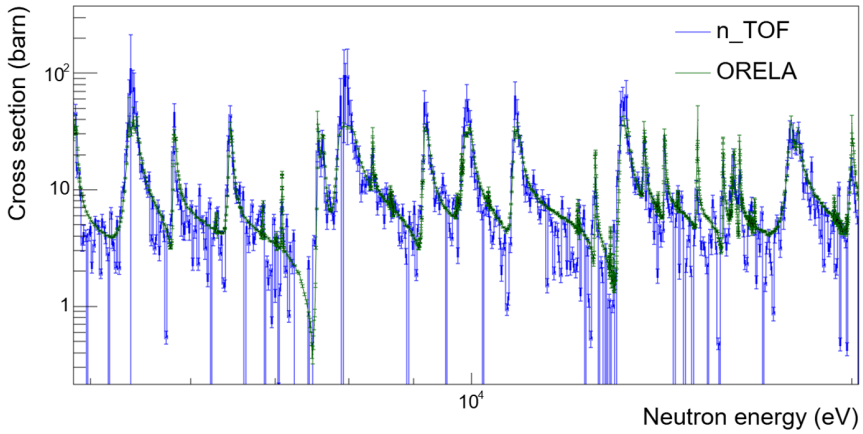

Figure 50: ^{nat}Cu(n,tot) cross section of n_TOF (in blue) and ORELA data (in green) - close up on the resonances around 10^4 eV.

50, a close up of the same plot on some resonances is presented. From this comparison, it is possible to observe a good agreement between the resonances measured by the two facilities. Furthermore, it is possible to notice that n_TOF resonances are measured with higher precision, as evidenced by their sharper structures.

A comparison was also performed with evaluated data from the CENDL-3.2 library [43]. In this case as well, a good agreement is found, especially in the resonance region, which is more clearly shown in Figure 52. Above 1 MeV, it is possible to appreciate the agreement of the inelastic contribution, confirming the consistency between the experimental data and the evaluated library also in this region.

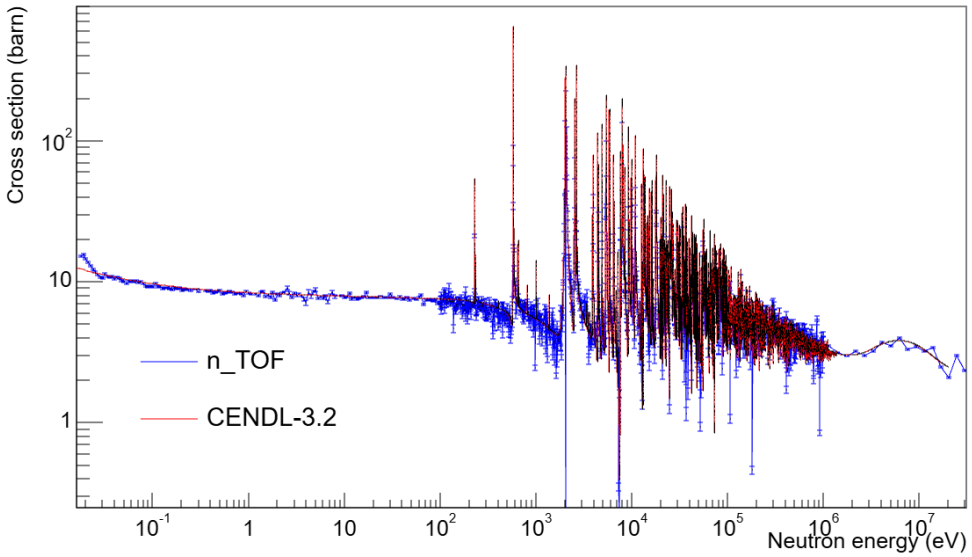

Figure 51: ^{nat}Cu(n,tot) cross section of n_TOF data (in blue) and evaluated data from CENDL-3.2 (in red).

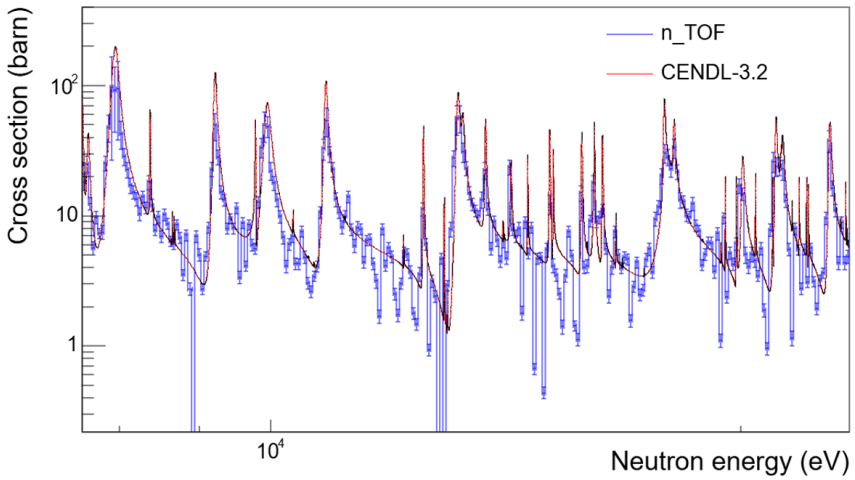

Figure 52: ^{nat}Cu(n,tot) cross section of n_TOF data (in blue) and evaluated data from CENDL-3.2 (in red) - close up on the resonances around 10^4 eV.

Conclusions

Motivated by the scarcity of experimental data and the inconsistencies observed in the evaluated data libraries for copper cross sections, considering also their relevance for the TAPIRO reactor, ENEA in collaboration with INFN proposed an experimental campaign for the refinement of neutron-induced copper cross sections through measurements at the n_TOF facility at CERN. The experimental campaign, named RAMEN, comprises the measurement of Cu(n,γ) and Cu(n,tot) cross section, performed in 2024, and 2025 respectively. The total cross section was measured by means of a transmission experiment, which was among the first of its kind at n_TOF. Transmission experiments can be used to determine the total cross section by measuring the neutron flux transmitted through a sample of the material under study and dividing it by the flux measured without it. A natural copper sample was used for this purpose, and the measurement was carried out at the n_TOF EAR1 experimental area. A Low Mass Fission Chamber (LMFC) detector, containing six ^{235}U samples, was employed for neutron detection and flux measurement. The events registered by the LMFC were acquired, processed, and analysed in detail.

The data analysis involved several optimization studies aimed at maximizing the quality of the extracted cross sections. First, the reconstruction of signals was improved by optimizing the parameters of the Pulse Shape Analysis routine. This work led, for some LMFC channels, to a reduction of noise at high energies and to an increase in statistics. Then, a detailed analysis of the amplitude distributions of the detected signals was carried out. From the analysis of the corresponding spectra, amplitude thresholds were defined for each channel in order to discriminate fission signals from background. The stability of the detector was monitored through the analysis of the position of the fission fragment amplitude distribution peak and the detection efficiency over time. These studies allowed the identification of some instabilities and the exclusion of the corresponding data from the analysis. Since no systematic shifts emerged from these studies, the detector was considered stable over the full duration of the measurement campaign. This analysis allowed the improvement of the accuracy and the assessment of the systematic uncertainty associated with the choice of an amplitude threshold. Finally, a comparison between amplitude spectra corresponding to high-intensity and low-intensity proton bunches was performed and led to a refinement of the selection conditions, improving the signal to noise ratio.

Furthermore, the time-of-flight analysis was performed on the same data set. The starting time information, required for the TOF computation, was extracted from the PKUP detector and then calibrated to match the γ-flash registered with the LMFC. Then, TOF histograms were built for Sample-in and Sample-out data and, from their ratio, transmission histograms were extracted. The compatibility of different datasets, corresponding to different LMFC channels, weeks of measurements, and neutron bunch

intensity, was assessed through a comparison of their TOF and transmission histograms. All datasets were found to be compatible within, typically, less than 5%.

Once the data sorting and selection was performed, a calibration of the flight path was needed to convert time-of-flight spectra to neutron kinetic energy spectra. The TOF-to-energy calibration was performed via a least-squares adjustment of the flight path, based on the analysis of several low-energy resonances in copper.

Finally, the total cross section as a function of neutron energy was extracted, applying the selection cuts and conditions established in the previous stages of the data analysis. The broad energy spectrum of the n_TOF neutron beam allowed the measurement of copper total cross sections over a wide energy range. Since the measurement was primarily motivated by the needs of the fast-spectrum TAPIRO reactor, a key objective was to extend reliable nuclear data to high energies, namely the MeV region. This goal was successfully achieved, with cross sections extending up to 30 MeV.

The extracted cross section shows good agreement in the resonance region with existing experimental data and evaluated libraries, highlighting the high quality of the n_TOF measurements and of the adopted analysis procedure. These results provide a significant contribution to the improvement of the nuclear data available for copper, forming a solid basis for advancements in reactor physics applications.

Acknowledgement

This project has received fundings from the European Union's Horizon Europe Research and Innovation programme under Grant Agreement No 101057511 (EURO-LABS).
This project has received fundings from the European Union's Horizon Europe Research and Innovation programme under Grant Agreement No 101164596 (APRENDE).

References

[1] Generation IV International Forum. https://www.gen-4.org, 2026.

[2] Igor L Pioro and Gilles H Rodriguez. Generation IV international forum (GIF). In *Handbook of Generation IV Nuclear Reactors*, pages 111–132. Elsevier, 2023.

[3] Generation IV International Forum. The Six Generation IV Nuclear Energy Systems. https://www.gen-4.org/generation-iv-criteria-and-technologies, 2024.

[4] International Atomic Energy Agency. World fusion outlook 2025. Technical report, International Atomic Energy Agency, Vienna, Austria, 2025.

[5] International Atomic Energy Agency. World survey of fusion devices 2022. Technical report, International Atomic Energy Agency, Vienna, Austria, 2022.

[6] ITER Organization. `https://www.iter.org`.

[7] M Angelone, D Flammini, S Loreti, F Moro, M Pillon, and R Villari. Copper benchmark experiment at the Frascati Neutron Generator for nuclear data validation. *Fusion Engineering and Design*, 109:843–847, 2016.

[8] Karolina Kolos, Vladimir Sobes, Ramona Vogt, Catherine E Romano, Michael S Smith, Lee A Bernstein, David A Brown, Mary T Burkey, Yaron Danon, Mohamed A Elsawi, et al. Current nuclear data needs for applications. *Physical Review Research*, 4(2):021001, 2022.

[9] Lee A Bernstein, David A Brown, Arjan J Koning, Bradley T Rearden, Catherine E Romano, Alejandro A Sonzogni, Andrew S Voyles, and Walid Younes. Our future nuclear data needs. *Annual Review of Nuclear and Particle Science*, 69(1):109–136, 2019.

[10] E Dupont, M Bossant, R Capote, AD Carlson, Y Danon, M Fleming, Zhigang Ge, Hideo Harada, O Iwamoto, N Iwamoto, et al. HPRL–International cooperation to identify and monitor priority nuclear data needs for nuclear applications. In *EPJ Web of Conferences*, volume 239, page 15005. EDP Sciences, 2020.

[11] B. Pritychenko, E. Běták, M.A. Kellett, B. Singh, and J. Totans. The Nuclear Science References (NSR) database and Web Retrieval System. *Nuclear Instruments and Methods in Physics Research Section A: Accelerators, Spectrometers, Detectors and Associated Equipment*, 640(1):213–218, 2011.

[12] Naohiko Otuka, Eea Dupont, V Semkova, B Pritychenko, AI Blokhin, M Aikawa, S Babykina, M Bossant, G Chen, S Dunaeva, et al. Towards a more complete and accurate experimental nuclear reaction data library (exfor): international collaboration between nuclear reaction data centres (nrdc). *Nuclear Data Sheets*, 120:272–276, 2014.

[13] M Salvatores and É Fort. Ameliorer et completer les donnees nucleaires indispensables aux neutroniciens. *CLEFS CEA*, 45:22–29, 2001.

[14] Luca Damele. Developement of ERANOS modules for the sensitivity analysis of the effective delayed neutron fraction beyond cross sections. Master's thesis, Alma Mater Studiorum – Università di Bologna, Bologna, Italy, 2025.

[15] OECD Nuclear Energy Agency (NEA). International Criticality Safety Benchmark Evaluation Project (ICSBEP) Handbook. `https://www.oecd-nea.org/jcms/pl_20291/international-criticality-safety-benchmark-evaluation-project-icsbep-handbook`, 2026.

[16] Giuseppe Palmiotti, J Blair Briggs, Teruhiko Kugo, Edward Trumble, Albert C Kahler, and Dale Lancaster. Applications of integral benchmark data. *Nuclear science and engineering*, 178(3):295–310, 2014.

[17] Technical datasheet of TAPIRO research reactor. `https://www.kep.enea.it/elenco-completo/impianti/reattore-di-ricerca-tapiro.html`, 2019.

[18] M Carta, P Console Camprini, V Fabrizio, O FIorani, A Grossi, V Peluso, A Santagata, A Boccia, A Gardini, C Bethaz, et al. TAPIRO: feasibility study of minor actinides irradiation campaign. *ENEA Report RdS*, 83, 2014.

[19] Fabrizio Pisacane, Luca Ricci, Alfonso Santagata, Augusto Gandini, Tommaso Murgia, Luca Cretara, Vincenzo Peluso, Massimo Sepielli, Mario Carta, Valentina Fabrizio, et al. The TAPIRO as a fast research reactor for Generation IV technologies. In *International Conference on Fast Reactors and Related Fuel Cycles: Safe Technologies and Sustainable Scenarios (FR13)*, 2013.

[20] Andrea Talamazzini. Il reattore nucleare TAPIRO: calcoli di sensibilità del fattore di moltiplicaizone efficace. Bachelor's thesis, Alma Mater Studiorum – Università di Bologna, Bologna, Italy, 2024.

[21] MS Pandey, JB Garg, and JA Harvey. Neutron total cross sections and resonance parameters of $^{63}_{29}Cu$ and $^{65}_{29}Cu$. I. *Physical Review C*, 15(2):600, 1977.

[22] K Kauwenberghs, Björn Becker, Jean Claude Drohe, K Guber, Stefan Kopecky, Peter Schillebeeckx, Danny Vendelbo, Ruud Wynants, et al. Results of time-of-flight

transmission measurements for ^{63,65}Cu and ^{nat}Cu at a 50 m station of GELINA. *Euratom Reports,(26479)*, 2013.

[23] RW Finlay, WP Abfalterer, G Fink, E Montei, T Adami, PW Lisowski, GL Morgan, and RC Haight. Neutron total cross sections at intermediate energies. *Physical Review C*, 47(1):237, 1993.

[24] Sofia Zalambani. Il reattore nucleare TAPIRO: valutazione dell'impatto delle sezioni d'urto del rame sui calcoli di criticità. Bachelor's thesis, Alma Mater Studiorum – Università di Bologna, Bologna, Italy, 2024.

[25] Michael Bacak, Marco Pignatari, Maria Diakaki, Cristian Massimi, Elisa Pirovano, Nicholas Terranova, Antonio Guglielmelli, Giacomo Grasso, Agatino Musumarra, Donato Maurizio Castelluccio, et al. Study of n + ^{63,65}Cu reactions and their relevance for nuclear technologies and Astrophysics. Proposal CERN/INTC-P-689, CERN, Geneva, Switzerland, 2024.

[26] Donato Maurizio Castelluccio, Alice Berardi, Patrizio Console Caprini, Giacomo Grasso, Cristian Massimi, Agatino Musumarra, Maria Grazia Pellegriti, Nicholas Pieretti, and Andrea Talamazzini. High-Precision and High-Accuracy Copper Nuclear Data for Fast Reactor Analyses. *Physor 2026*. Submitted and accepted.

[27] APRENDE Project. Addressing PRiorities of Evaluated Nuclear Data in Europe. `https://aprende-project.eu/`.

[28] N Colonna, F Gunsing, and F Käppeler. Neutron physics with accelerators. *Progress in Particle and Nuclear Physics*, 101:177–203, 2018.

[29] Alberto Mengoni, Paolo Maria Milazzo, and Nikolas Patronis. n_TOF at CERN: Status and Perspectives. *Nuclear Physics News*, 34(3):26–29, 2024.

[30] Ewa Lopienska. The CERN accelerator complex, layout in 2022. 2022.

[31] N Patronis, A Mengoni, S Goula, O Aberle, V Alcayne, Saverio Altieri, S Amaducci, Józef Andrzejewski, V Babiano-Suarez, M Bacak, et al. Status report of the n_TOF facility after the 2nd CERN long shutdown period. *EPJ Techniques and Instrumentation*, 10(1):1–10, 2023.

[32] Raffaele Esposito and Marco Calviani. Design of the third-generation neutron spallation target for the CERN's n_TOF facility. *Journal of Neutron Research*, 22(2-3):221–231, 2020.

[33] Raffaele Esposito, Marco Calviani, Oliver Aberle, Massimo Barbagallo, Daniel Cano-Ott, T Coiffet, N Colonna, César Domingo-Pardo, Francesco Dragoni, R Franqueira Ximenes, et al. Design of the third-generation lead-based neutron spallation target for the neutron time-of-flight facility at CERN. *Physical Review Accelerators and Beams*, 24(9):093001, 2021.

[34] Carlos Guerrero, Andrea Tsinganis, E Berthoumieux, M Barbagallo, F Belloni, F Gunsing, Christina Weiß, Enrico Chiaveri, M Calviani, V Vlachoudis, et al. Performance of the neutron time-of-flight facility n_TOF at CERN. *The European Physical Journal A*, 49(2):27, 2013.

[35] Christina Weiß, Enrico Chiaveri, Sylvain Girod, Vasilis Vlachoudis, O Aberle, S Barros, I Bergström, E Berthoumieux, M Calviani, C Guerrero, et al. The new vertical neutron beam line at the CERN n_TOF facility design and outlook on the performance. *Nuclear Instruments and Methods in Physics Research Section A: Accelerators, Spectrometers, Detectors and Associated Equipment*, 799:90–98, 2015.

[36] Marta Sabate-Gilarte, Massimo Barbagallo, Nicola Colonna, F Gunsing, P Žugec, V Vlachoudis, YH Chen, Athanasios Stamatopoulos, Jorge Lerendegui-Marco, Miguel Antonio Cortés-Giraldo, et al. High-accuracy determination of the neutron flux in the new experimental area n_TOF-EAR2 at CERN. *The European Physical Journal A*, 53(10):210, 2017.

[37] Matteo Ferrari, Dominika Senajova, O Aberle, YQ Aguiar, D Baillard, Massimo Barbagallo, A-P Bernardes, L Buonocore, Matteo Cecchetto, Vincent Clerc, et al. Design development and implementation of an irradiation station at the neutron time-of-flight facility at CERN. *Physical Review Accelerators and Beams*, 25(10):103001, 2022.

[38] Massimo Barbagallo, C Guerrero, Andrea Tsinganis, D Tarrío, S Altstadt, S Andriamonje, J Andrzejewski, L Audouin, V Bécares, F Bečvář, et al. High-accuracy determination of the neutron flux at n_TOF. *The European Physical Journal A*, 49(12):156, 2013.

[39] A. Manna, E. Pirovano, O. Aberle, S. Amaducci, M. Barbagallo, D.M. Castelluccio, N. Colonna, P. Console Camprini, L. Cosentino, M. Dietz, Q. Ducasse, P. Finocchiaro, C. Le Naour, S. Lo Meo, M. Mastromarco, C. Massimi, A. Mengoni, P.M. Milazzo, F. Mingrone, R. Nolte, M. Piscopo, D. Radeck, M. Spelta, L. Tassan-Got, N. Terranova, G. Vannini, and on behalf of the n_TOF collaboration. Recoil Proton Telescopes and Parallel Plate Avalanche Counters for the 235U(n,f) cross section measurement relative to H(n,n)H between 10 and 450 MeV neutron energy. *Journal of Instrumentation*, 18(04):P04024, apr 2023.

[40] E Pirovano, A Manna, O Aberle, S Amaducci, N Colonna, P Console Camprini, L Cosentino, M Dietz, Q Ducasse, P Finocchiaro, et al. A detector system for absolute measurements of fission cross sections at n_TOF in the energy range below 200 MeV. *Journal of Instrumentation*, 18(11):P11011, 2023.

[41] Cristian Massimi. Lecture Slides for Nuclear Physics. Course lectures, University of Bologna, 2023.

[42] David Brown. Release of the ENDF/B-VII. 1 evaluated nuclear data file. Technical report, 2012.

[43] Zhigang Ge, Ruirui Xu, Haicheng Wu, Yue Zhang, Guochang Chen, Yongli Jin, Nengchuan Shu, Yongjing Chen, Xi Tao, Yuan Tian, et al. CENDL-3.2: The new version of Chinese general purpose evaluated nuclear data library. In *EPJ Web of Conferences*, volume 239, page 09001. EDP Sciences, 2020.